UNIVERSIDAD DE CHILE
FACULTAD DE CIENCIAS FÍSICAS Y MATEMÁTICAS
DEPARTAMENTO DE ASTRONOMÍA

THE CIRCUMGALACTIC MEDIUM OF HIGH-z GALAXIES: C IV AND Si IV ABSORPTION LINE STUDIES AROUND z $\sim$ 2−3 GALAXIES

TESIS PARA OPTAR AL GRADO DE

MAGISTER EN CIENCIAS, MENCIÓN ASTRONOMÍA

AMBER ROBERTS

PROFESOR GUÍA:
DR. GUILLERMO BLANC MENDIBERRI

MIEMBROS DE LA COMISIÓN:
DR. GWEN RUDIE
DR. VALENTINO GONZALEZ CORVALAN
DR. LAURA PEREZ MUÑOZ

SANTIAGO DE CHILE
2019

RESUMEN DE LA MEMORIA PARA OPTAR
AL TÍTULO DE MAGISTER EN CIENCIAS, MENCIÓN ASTRONOMÍA
POR: AMBER ROBERTS
FECHA: 2019
PROF. GUÍA: DR. GUILLERMO BLANC MENDIBERRI

THE CIRCUMGALACTIC MEDIUM OF HIGH-z GALAXIES: C IV AND Si IV ABSORPTION LINE STUDIES AROUND z $\sim$ 2−3 GALAXIES

Understanding the baryonic interaction between the star-forming galaxies and their surrounding gaseous haloes is key to deciphering the processes of galaxy formation and evolution. We present the results of Keck Baryonic Structure Survey (KBSS), an ideal spectroscopic study to observe metal absorption line systems at scales of $\sim$ 50 kpc − 1.5 Mpc of galaxies L* at z$\sim$ 2. In this work, we use KBSS data for 15 hypersoiling QSOs in z $\sim$ 2.5−2.9 as background sources to search for the gas surrounding 711 foreground galaxies selected by UV at $2 \leq z \leq 2.8$. All 711 galaxies that form KBSS stars are <1.5 of physical Mpc of the QSO line of sight, with QSO spectra of the Keck / HIRES instrument having S / N $\sim$ 100 Keck / HIRES, ensuring a detailed analysis of the metal absorption characteristics.

The absorption lines of C IV and Si IV probe the presence of metals in the circumalctic medium (CGM) of galaxies, and are fundamental to trace the history of the baryonic cycle of a galaxy. In this thesis, we used the Voigt profile adjustment to evaluate the column densities, relative velocities and velocity profiles of metal absorbers C IV and Si IV in the ionized halo gas in the physical impact parameters < 1500 pkpc , to investigate the kinematics and structure of the highly ionized gas that surrounds galaxies.

From our results that observe the statistics of the coverage fraction and the sum as a function of the impact parameter, we show conclusive evidence that the absorption of C IV and Si IV along the QSO lines of vision correlates with the presence of galaxies. The probability of seeing this absorption increases rapidly with increasing proximity to galaxies, since the absorbents of C IV and Si IV are grouped with galaxies. The measurement of metal distributions and gas flows is crucial to understanding the baryonic processes that are key to improving our understanding of galaxy formation.

Comprender la interacción bariónica entre las galaxias formadoras de estrellas y sus halos gaseosos circundantes es clave para descifrar los procesos de formación y evolución de galaxias. Presentamos los resultados de Keck Baryonic Structure Survey (KBSS), un estudio espectroscópico ideal para estudiar sistemas de líneas de absorción de metales en escalas de $\sim$ 50 kpc − 1.5 Mpc de las galaxias L * a $z \sim 2$. En este trabajo, usamos datos KBSS para 15 QSO hiperluminosos en z $\sim$ 2.5−2.9 como fuentes de fondo para buscar el gas que rodea a 711 galaxias en primer plano seleccionadas por UV a $2 \leq z \leq 2.8$. Todas las 711 galaxias que forman estrellas KBSS son < 1.5 de Mpc físico de la línea de visión QSO, con espectros QSO del instrumento Keck / HIRES que tienen S / N $\sim$ 100 Keck / HIRES, asegurando un análisis detallado de las características de absorción metálica. .

Las líneas de absorción de C IV y Si IV sondean la presencia de metales en el medio circunaláctico (CGM) de las galaxias, y son fundamentales para rastrear la historia del ciclo bariónico de una galaxia. En esta tesis, utilizamos el ajuste del perfil de Voigt para evaluar las

densidades de columna, las velocidades relativas y los perfiles de velocidad de los absorbedores de metal C IV y Si IV en el gas halo ionizado en los parámetros de impacto físico < 1500 pkpc, para investigar la cinemática y la estructura del gas altamente ionizado que rodea a las galaxias.

A partir de nuestros resultados que observan las estadísticas de la fracción de cobertura y la suma como una función del parámetro de impacto, mostramos evidencia concluyente de que la absorción de C IV y Si IV a lo largo de las líneas de visión QSO se correlaciona con la presencia de galaxias. La probabilidad de ver esta absorción aumenta rápidamente al aumentar la proximidad a las galaxias, ya que los absorbentes de C IV y Si IV están agrupados con galaxias. La medición de las distribuciones metálicas y los flujos de gas es crucial para comprender los procesos bariónicos que son clave para mejorar nuestra comprensión de la formación de galaxias.

This study of C IV goes out to all the carbon-based lifeforms.

Acknowledgements

I would first like to thank my family for their continued support throughout my academic career. In particular my mom for her constant praise when I succeed and even when I fail. My dad for coming down to Chile with me when I first moved here, and always showing an active interest in my studies and research. My parents have given me every opportunity to find and pursue my passions and I am very grateful to them for belief in me.

I would also like to thank the friends in my life, especially my fellow graduate students at Calan: Nina, Gus, Mari, Paula, Blake, Mati, Elise, Suafle, Coni, Jorge, Grecco, Seba, Sudeep, Jose, Ricardo and Juanpi. My chica Liz for our fantastic study sessions and my boyfriend Billy for always making the stressful times easier. They have all helped me tremendously in adjusting to a new culture, as well as developing my skills as a researcher.

I would like to thank the members of my committee: Laura, Valentino, Gwen, and Guillermo, for helping to revise my thesis. I would acknowledge Gwen and Guillermo individually for the crucial role they played in getting me to where I am today. It was been a privilege to be advised by Gwen. She is a fantastic role model for any aspiring astronomer, as she has the passion, focus, and gold standards both in research and educational outreach that we all in academia should strive to reach. She constantly pushed me to be produce my best work and think critically about the findings presented in this thesis. Guillermo was the enthusiastic voice that led me to come to Chile, his excitement for the work we were doing was truly contagious and it was a pleasure to be his student. He presented me with opportunities that proved to myself my capabilities as an astronomer.

Lastly, I would like to thank the Department of Astronomy at the Universidad de Chile for accepting me into their program, as well as The Carnegie Observatories in Pasadena, CA for granting me a year long graduate student Fellowship and giving me the opportunity to study at the same institution where Hubble first discovered the expansion of the Universe.

Contents

List of Figures

Introduction

Less than a few hundred million years after the Big Bang, gas in the early universe began to accrete onto dark matter halos and cool to the point of forming the first galaxies. A couple billion years later at z= 2−3, stars were forming at a 30 times greater rate than it is seen around us today (Madau et al. 2014). The star formation rate density was at an all time high and with all this star formation activity, the rate of black hole growth at the centers of galaxies was also at its height.

Before stars can actually form, gas must be accreted onto the dark matter halos and cool within the interstellar medium (ISM). While inflowing gas is being gravitationally drawn into the centers of galaxies, the gas is battling various feedback mechanisms in order to make its way through the halos. Galactic winds have been observed to blow gas away from the disks of galaxies and expand to at least the virial radius of their halos (r_{vir}) as seen in absorption by Steidel et al (2010). These outflows are generated by feedback from star-formation and active galactic nuclei (AGN), and we are interested in studying various forms of feedback because these are the processes responsible for ejecting metals into the ISM, circumgalactic medium (CGM), and intergalactic medium (IGM). Outflowing ISM gas must deposit its heavy elements at large distances in order to achieve the observed abundance of metals that we see in the CGM (Werk et al. 2014, Tumlinson et al. 2011, Steidel et al. 2010, Tripp et al. 2012, Chen et al. 2001).

When gas gets ejected from the metal enriched ISM of a galaxy due to various forms of feedback it could be fully ejected out to the IGM via outflows, or could be ejected from the ISM, but remain bound to the galaxy to eventually fall back onto it. This second scenario signifies that the gas will eventually be recycled and reaccreted back onto the host galaxy. The "galaxy baryon cycle" describes the inflow and outflow of gas, its transformation into stars, its ejection from the galaxy through winds, and perhaps its eventual return to the ISM (Faucher-Giguère et al. 2011, Ford et al. 2014, Christensen et al. 2016, Muratov et al. 2016) for the refueling of star formation (Oppenheimer et al. 2010). This process is repeated for billions of years to feed the baryon cycle and the growth of galaxies.

In star forming galaxies, galactic winds are a result of the energy injected by young massive stars and supernovae. These galactic winds transport metals around the ISM, within the CGM of galaxies, and even out into the IGM, to modulate the chemical evolution of galaxies. While the assertion that galactic winds enrich the IGM with metals has been well established, the conditions responsible for the creation of these winds are not clearly understood. The properties and scales responsible for creating galactic winds still need to be constrained by

high resolution observations of the IGM and CGM, as well as state-of-the-art cosmological simulations.

Modeling galaxy accretion (Kereš et al. 2005, Brooks et al. 2009, Dekel et al. 2009, Kereš et al. 2009a, Faucher-Giguère et al. 2011, van de Voort et al. 2011) and inflowing gas from filament structures present in the IGM, helps us understand how gas is passed, pushed and propelled in and out of galaxies (Oppenheimer & Davé 2006, 2008, Aguirre et al. 2001a,b, Tescari et al. 2011, Wiersma et al. 2010, 2011, Anglés-Alcázar et al. 2014, Muratov et al. 2015, 2016), and how previously ejected gas in galactic winds is reaccreted back onto the galaxy to form stars (Shapiro & Field 1976, Oppenheimer et al. 2010, Anglés-Alcázar et al. 2017). Recycled accretion arises from the ejection of metal-enriched galactic winds that lack the energy to escape the halo entirely, or which encounter the CGM itself and lose energy to radiation from shocks and then eventually cool and re-enter the galaxy (Tumlinson et al. 2017 and Heckman et al. 2017).

Theoretical simulations suggest that these processes are taking place, and have an estimation of the amount of material present in gas being recycled, but a question still remains of how feedback actually regulates the formation of galaxies and how gas accretion affects the rate at which galaxies form stars. Hydrodynamic simulations give a means to test ideas about the underlying physical processes that drive feedback and/or star-formation regulation to paint a picture of galaxy formation, but until we make actual observations which demonstrate that we have captured the relevant physics, we don't actually know how gas accretion affects galaxies or if most of the metals recycle or don't recycle.

Taking a look at the multiphase CGM through hydrodynamic simulations, we find a mixture of cool (10^4 K) and warm-hot ($10^{5.5}$ K-10^6 K) gas and a density profile that drops with increased distance from the central host galaxy (Shen et al. 2013, Stinson et al. 2012, Ford et al. 2013, Suresh et al. 2017). The accepted picture of galaxy assembly is based on the predictions made in cosmological simulations, ranging from modeling the cold accretion of gas through filaments that never shock heat to virial temperature, to gas shock heated to virial temperatures before cooling and condensing to form stars (Keres et al. 2005, 2009, Oppenheimer et al. 2010, Faucher-Giguere et al. 2011, Van de Voort et al. 2011, Nelson et al. 2013, Dekel et al. 2009), both of these hot and cold accretion models are believed to occur at $z > 2$.

In order to test the validity of these simulations we need in depth observations of IGM and CGM gas at a variety of distances from galaxies, as well as a concurrent analysis of the metal content of that gas. Since gas exists not only inside of galaxies within the ISM, but also closely around galaxies within the CGM, as well as outside the halos in the IGM, we require observations of gas in all of these spaces in order to have a holistic view of the baryon cycle.

The gas making up the ISM of galaxies can be easily studied in emission across multiple wavelengths ranging from the UV to the FIR/radio. However, gas in the CGM/IGM that exists in and around the halos of galaxies is not so easily observed, in fact it is extremely difficult to detect this gas in emission and we therefore need to see this gas in absorption against background sources. Since QSOs are one of the brightest objects in the universe, using them as a background source is ideal for probing gas at cosmological distances. When

we look at QSO spectra we notice a significant amount of absorption along the line of sight as light from the QSO passes through gas on its way to us. By harnessing this technique known as quasar absorption line (QAL) spectroscopy we can analyze the absorbers and derive the chemical structure of the intervening halos of galaxies.

The technique of QAL spectroscopy has been implemented as early as Bahcall, Peterson & Schmidt (1966). The sophistication of the QAL technique really matured in the field starting in the 1980's, concurrently with advancement in telescopes. While metal lines from halo gas are mostly impossible to constrain in emission, they can be detected through the use of far-UV absorption-line spectroscopy of background QSOs to observe the IGM (Rauch, Carswell, and Sargent 2012, H.W. Chen & Cowie 2009) as well as the CGM (Tripp et al. 2008, Wakker & Savage 2009, Prochaska et al. 2011a, Tumlinson et al. 2011, Rudie et al. 2012, Savage et al. 2014, Werk et al. 2016). Since metals are seen in random directions in the IGM, and metals have long been thought to be associated with galaxies, the next step became mapping the IGM along sightlines that pass very close to galaxies. While QAL spectroscopy was first used to study the properties and distribution of gas in IGM, the ionized CGM of foreground galaxies can be detected through rest-frame UV absorption lines (Bahcall & Spitzer 1969, Bergeron 1986, Tripp et al. 2000, Chen et al. 2001, Prochaska et al. 2006).

With hydrogen being the most abundant element in our universe and making up over 90% of the total atoms in the early universe, neutral hydrogen (H I) was the first element to be studied in depth in the CGM at high$-z$, complementing low$-z$ H I CGM studies within 200 kpc of galaxies (Chen et al. 2001, Bowen et al. 2002, Penton et al. 2002, Wakker & Savage 2009, Tumlinson 2014). Diffuse CGM gas is mainly traced by H I (Morris et al. 1993, Lanzetta et al. 1995) and when previous studies looked at LBGs in a redshift survey at z $\sim$ 3, the excess H I absorption could be seen extending out to $\sim$ 1 comoving physical Mpc (pMpc) from their host galaxy (Adelberger et al. 2003, 2005a).

Rudie et al. (2012) then greatly increased our current understanding of the physical properties that govern H I at these epochs with the finding that the probability of encountering a $N_{HI} \geq 10^{14.5}$ cm^{-2} absorber within 300 pkpc, within $\pm$ 350 km s^{-1} of the galaxy redshift, is > 4 times greater than at random places in the IGM, signaling the presence of a gas rich CGM around galaxies. H I gas was also found to have excess absorption, at a lower level, out to a few pMpc distance away from z $\sim$ 2.5 star forming galaxies (Rudie et al. 2012). This finding is indicative of large scale structure and the fact that these galaxies at $2.0 \leq z_{gal} \leq 2.8$ on average sit in high density regions in our universe. The interesting topic of discussion was whether or not these systems were due to randomly intervening intergalactic H I gas (uninfluenced by the presence of galaxies) or was due to the clustering of galaxies (and their associated CGM) unaccounted for in the Rudie et al. (2012) sample. We use this knowledge of H I as the dominant source of gas in the CGM to provide a critical basis for our study of the C IV and Si IV absorption in the high$-z$ CGM.

Metal absorption has been seen in the IGM through the use of background QSOs across a very broad redshift range implying that at least parts of the IGM are metal enriched. Since carbon and silicon were not present at the time of the Big Bang, we can infer that these metals formed in stars inside galaxies and were likely ejected by galaxies. However, we don't know how far out can these metals travel, if they get mixed with the bulk of the IGM, or

how concentrated they are near the CGMs of galaxies.

The existence of highly ionized, metal absorption in the IGM of the early universe was first seen in C IV absorption associated with z $\sim$ 3 Lyα forest absorbers in high-resolution optical spectra (Cowie et al. 1995, Songaila & Cowie 1996, Cowie & Songaila 1998). In addition to the metal transitions of C IV, Si IV has also been used in high redshift observation of metal absorption in the IGM (Steidel 1990, D'Odorico et al. 2010, Simcoe et al. 2011, Cooksey et al. 2010, 2013, Bordoloi et al. 2017). Both C IV $\lambda\lambda$1548, 1550 and Si IV $\lambda\lambda$1394, 1403 are often selected for their sensitivity to enriched gas, ability to trace the metallicity in the high$-z$ IGM, their easily identifiable doublet transitions (as long as the resolution of the spectra is high enough to resolve the doublet) and the fact that C IV (which redshifts into the optical at z $>$ 1.5) and Si IV both lie redwards of the Lyα forest and therefore avoid unwanted contamination from H I.

The C IV doublet is one of the most commonly used absorption lines to trace metals in the IGM from z $>$ 5 to today (Steidel 1990, Danforth & Shull 2008, D'Odorico et al. 2010, Simcoe et al. 2011, Cooksey et al. 2010, 2013, Bordoloi et al. 2017). The first C IV measurements at z $\sim$ 6 were made by (Simcoe et al. 2006) and (Ryan-Weber, Pettini, & Madau 2006), and show that the presence of C IV in the IGM of the high$-z$ universe indicates heavy-element enrichment began $\leq$ 1 Gyr after the Big Bang.

Building on these results, Ryan-Weber et al. (2009) demonstrated a decrease in the frequency of C IV absorption at z $\sim$ 6. This result was drawn from the lack of C IV doublets detected, which should have been readily found if the column density distribution of C IV absorbers remained invariant from 1.5 $\leq$ z $\leq$ 4.5 (Ryan-Weber et al. 2009). Simcoe et al. (2011) used the FIRE spectrograph to show consistent evidence of a decline in C IV abundance at z $>$ 5.

Studies aimed to understand the properties of the C IV doublet have also studied the Si IV doublet due to Si IV presence being associated with findings of C IV. D'Odorico et al. (2013) used both C IV and Si IV absorption to investigate the metal content of QSO absorbers at z $>$ 4.35 and put further constraints on the nature of absorbers. We have seen evidence to suggest C IV absorbers are correlated with the presence of galaxies near the QSO line of sight (Steidel et al. 2010 and Adelberger et al. 2008). Boksenberg and Sargent (2015) found that the C IV absorber components, outside the Lyman forest over $1.6 < z < 4.4$, exhibit strong clustering out to velocity separations 300 km s^{-1}. This could be due to the peculiar velocities of gas present in the outer extensions of galaxies being probed in the confined sightlines to the background QSOs, which in general do not encounter more than one galaxy in a given cluster or group (Boksenberg and Sargent, 2015). In this work we consider highly ionized gas from C IV and Si IV and their relations to the CGMs of nearby galaxies.

At high$-z$, complex C IV absorption systems in the CGM are commonly observed at similar redshifts to those of galaxies close to the QSO sighlines (Steidel et al. 2010, Martin et al. 2010 Adelberger et al. 2003, 2005). In 2010, Charles Steidel and collaborators characterized the C IV absorption around 512 high$-z$ ($z < 2.2$) foreground galaxies at physical impact parameters less than 125 pkpc. From the stacked spectra from galaxy-galaxy pairs they found the mean C IV absorption strength falls off rapidly with increasing galactocentric impact parameters from 50 pkpc to 100 pkpc. Prochaska et al. (2013a) studied the CGM

using quasar-quasar pairs (instead of foreground galaxies-background quasar pairs or Steidel's foreground galaxy-background galaxy pairs) to show that quasars exhibit significantly stronger C IV as compared to LBGs at similar redshifts, especially at impact parameters greater than 100 pkpc.

Metal absorption of O VI, N V, C IV, C III, and Si IV around $z \sim 2.5$ galaxies had been previously studied using statistical methods by Turner et al. (2014), where the "pixel optical depth"(POD) was to study the $2-$D metal distribution around the galaxies. Turner et al. (2014) found that for C IV (and H I) there was a significant enhancement of the absorption signal out to 2 pMpc in the transverse direction (the maximum impact parameter in their sample). The POD method (Turner et al. 2014, Cowie& Songaila 1998, Songaila 1998, Ellison et al. 2000, Schaye et al. 2000, Aguirre et al. 2002, Schaye et al. 2003) is a useful way to take an efficient, objective, statistical measurement of a highly contaminated region of QSO spectra by comparing the Lyα optical depth in each pixel with the optical depth in the pixel at the corresponding metal-line wavelength (Aguirre et al. 2002). While the POD method allows for an efficient measurement of absorption strengths, we need to get actual column densities for high redshift metal ions if we want to understand the detailed physical and chemical structure of the high$-z$ CGM.

In this work, we present the first detailed study of the spatial and kinematic distributions of C IV and Si IV gas around galaxies at high redshift ($z \approx 2-3$). Our work provides strong evidence that metal absorption is associated with the presence of galaxies. We show that the prospects for studying the distribution of metals in the CGM and IGM are largely improved by the availability of galaxy redshift surveys like the Keck Baryonic Structure Survey (KBSS), which sample the volumes in the foreground of bright background QSOs. Currently, our study is the best characterization of the spatial, as well as kinematic structure of metal absorption lines in the CGM as a function of distance from galaxies.

We present our results from the study of the distribution of C IV and Si IV absorption in terms of both space and velocity. We use Voigt profile fitting to assess the column densities, relative velocities, and velocity profiles of the ionized gas at physical impact parameters, $D_{Tran} < 1500$ pkpc, in order to investigate the kinematics and structure of the highly ionized gas that surrounds galaxies. The chapters are organized as follows, Chapter 1 outlines the data that we will be using, Chapter 2 details our measurements and analysis methods, and Chapter 3 dives into our results. Finally, we provide our Conclusions regarding the metal gas enhancement surrounding high$-z$ galaxies.

Chapter 1

Data: The Keck Baryonic Structure Survey

The data used in this thesis are drawn from the Keck Baryonic Structure Survey (KBSS; Steidel et al. 2010, Turner et al. 2014, Rudie et al. 2012) which was designed specifically to study the distribution of gas and metals in the circumgalactic medium (CGM) of galaxies. KBSS is a spectroscopic survey of galaxies and absorption systems conducted across the fields surrounding 15 hyper-luminous QSOs (over a total area of 0.24 deg^2).

The 15 hyper-luminous ($L_{bol} \geq 10^{14} L_{\odot}$) QSOs were observed with the High Resolution Echelle Spectrometer (HIRES; Vogt et al. 1994) on the Keck I telescope. KBSS combines the 15 Keck/HIRES QSOs to act as background sources at $2.5 \leq z_{QSO} \leq 2.85$ for photometrically selected star-forming foreground galaxies at $2.0 \leq z_{gal} \leq 2.8$. By using quasar absorption line spectroscopy we detect the presence of gas around galaxies at the peak of cosmic star formation (Reddy et al. 2008, Rudie et al. 2012).

The galaxy spectra were obtained at the W. M. Keck Observatory using the Low Resolution Imaging Spectrometer (LRIS, Oke et al. 1995; Steidel et al. 2004) and the Multi-object Spectrometer for Infrared Exploration (MOSFIRE, McLean et al. 2012; Steidel et al. 2014). The full KBSS sample includes 2844 UV color selected (Lyman-break) galaxies. Of these, 2345 galaxies have rest-frame UV spectra from LRIS and 1103 galaxies have rest-frame-optical spectra from MOSFIRE.

1.1 QSO spectra

The final HIRES QSO spectra have $R \simeq$45,000 (FWHM $\simeq$7 km s^{-1}), S/N $\sim$ 50–200 pixel^{-1}, roughly covering the 3100–6000 Å wavelength range. For a detailed description of the HIRES data acquisition and data reduction see Rudie et al. 2012. The QSO redshifts are measured from rest-frame optical emission lines using lower-dispersion NIR spectra as detailed in Trainor & Steidel (2011).

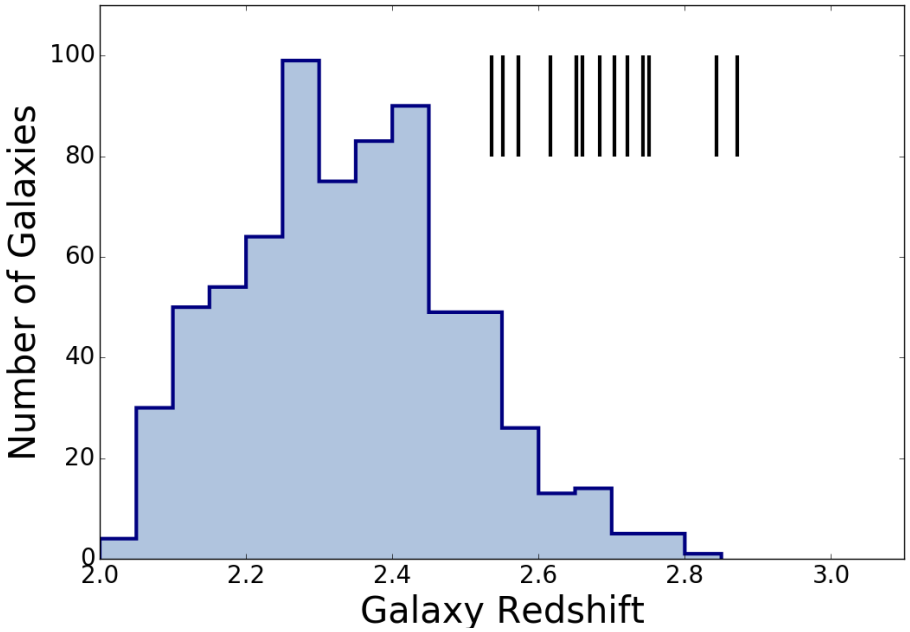

Figure 1.1: Redshift distribution of the 711 foreground galaxy redshifts from the KBSS subset which fall within <1.5 physical Mpc from the QSO line of sight. The black vertical line segments mark the redshifts of the 15 KBSS HIRES background QSOs, note that several QSOs redshifts overlap.

1.2 Galaxy Sample

In this work, we consider galaxies at redshifts where the HI Lyα, Lyβ, C IV, and Si IV transitions fall within the wavelength range of the QSO spectra. Specifically, we consider galaxies with $z_{gal} < z_{QSO} - 3000$ km s^{-1} (Rudie et al. 2012) to avoid using systems compromised by the ionizing radiation field of the host QSO or associated with the QSO itself. While the full KBSS galaxy sample contains more than 2000 galaxy redshifts we used a subset of 711 foreground galaxies satisfying the previous condition and falling within a < 1.5 physical Mpc [pMpc] distance from the QSO line-of-sight (LOS) as projected on the sky. The redshift distribution of the galaxy sample used in this work can be seen in Figure 1.1, where the black vertical lines correspond to the 15 Keck HIRES background QSOs. In our data we have 537 galaxies with redshifts measured from rest-UV spectroscopy from Keck/LRIS and 390 galaxies with redshifts measured from rest-optical spectroscopy from Keck/MOSFIRE.

For the 321 galaxies observed with both instruments, we used the MOSFIRE calibrated redshifts due to the redshift precision being Δv $\approx$ 18 km s $^{-1}$, compared with LRIS redshift precision of Δv $\approx$ 150 km s^{-1}. The properties of a typical galaxy in the KBSS survey are: the galaxies have apparent magnitudes of $m_R \leq 25.5$ and bolometric luminosities of $\sim 2.5\times10^{11} L_\odot$ (Reddy et al. 2008, 2012), with a corresponding median star forming rate of $\sim 25 M_\odot$ yr^{-1} (Strom et al. 2017) and a gas-phase metallicity of $Z_\odot/Z_\odot \simeq 0.3-0.9$ (Strom et al. 2017). These galaxies have average stellar masses $\sim 1\times10^{10} M_\odot$, and inhabit dark matter haloes of average mass $\sim 10^{12} M_\odot$, which were calculated from studying the the correlation

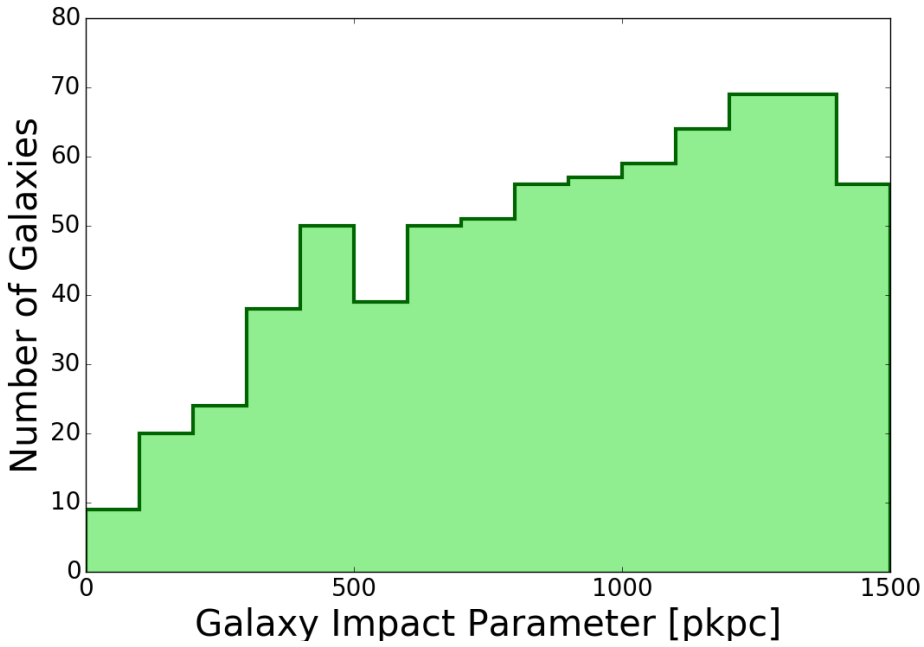

Figure 1.2: Number of galaxies as a function of physical impact parameter to the associated QSO for the 711 galaxies shown in Figure 1.1, which are within <1.5 physical Mpc from the QSO line of sight.

function from the clustering of galaxies (Adelberger et al. 2005b, Conroy et al. 2008, Trainor & Steidel 2011, O. Rakic et al. 2012). The details of the galaxy selection criteria are outlined in Steidel et al. (2004) and Adelberger et al. (2004).

Since these high-redshift galaxies are in the peak epoch of star formation and their spectral energy distributions (SEDs) are dominated by a star forming stellar populations with ages ~ 0.2 Gyr (R. Theios et al 2018,in prep). The luminous parts of the galaxies are dominated (in terms of mass) by baryons, typically half stars and half cold gas (Shapley et al. 2005, Erb et al. 2006c), with half-light radii of 2 pkpc (Law et al. 2012).

We consider galaxies within 1.5 pMpc of the QSO LOS in all 15 KBSS fields. The distribution of galaxies as a function of physical impact parameters between the galaxies and the QSO lines of sight is presented in Figure 1.2.

1.3 Calibrated Galaxy Redshifts

The multi-object near-infrared (NIR) spectrometer MOSFIRE sits at the Cassegrain focus of the Keck I telescope and operates over a field of view of 6.1' x 6.1', which covers nearly all atmospheric bandwidths for slits placed anywhere within the field (McLean 2012). MOSFIRE ($R \approx 3600$) data provides high precision redshifts for young, star forming galaxies by detailing the galaxy's nebular emission lines in the spectra. These emission lines trace the ionized gas in a galaxy's H II regions, which convey the systemic velocity of stars with high accuracy.

When using the galaxies star-forming regions as tracers of the systemic velocity of stars we take the galaxy's systemic redshift to be equal to the nebular emission line redshift ($z_{\rm gal}$ = $z_{\rm H\alpha}$). The MOSFIRE spectroscopic redhsifts of our galaxies have a typical uncertainty of $\Delta v \simeq 18$ km s^{-1}.

Complementary to MOSFIRE, is the dual-beamed optical spectrograph LRIS. LRIS is a visible-wavelength imaging and spectroscopy instrument that also operates at the Cassegrain focus of the Keck I telescope. LRIS has both red and blue cameras that can be operated simultaneously to generate a spectra with a total wavelength coverage of 3200–10,000 Å . The field of view in both modes of operation is 6' × 7.8'. Once light is collected, it is separated via beamsplitters into red and blue wavelengths of light. We use LRIS data from the blue arm, or the LRIS-B spectrograph, which covers the spectral range 3750 – 5200 Å at a resolving power $R \approx 800 - 1300$ (5–10 Å) (Rockosi et al. 2010, Oke et al. 1995). In this setup LRIS-B disperses blue light using a 400 line mm^{-1} grism at a typical spectral resolution FWHM $\simeq$ 370 km $^{-1}$ ($\sigma_{res} \simeq 160$ km $^{-1}$, Steidel 2004, 2010).

LRIS redshifts are determined from either the Lyα emission line ($z_{\rm Ly\alpha}$) or from interstellar (IS) metal absorption lines ($z_{\rm IS}$) , which are the most prominent features in the rest-frame UV spectra. However, the Lyα and interstellar (IS) absorption lines are typically redshifted and blueshifted from the systemic redshift of the galaxy (by several hundred km s $^{-1}$; Shapley et al. 2003, Adelberger et al. 2003, and Steidel et al. 2010) due to resonant scatter effects and outflowing winds respectively, and must be corrected to infer the system redshift. These shifts are important when studying the kinematics of the CGM because Lyα and the IS lines provide a biased measure of the systemic redshifts.

KBSS galaxy redshifts were obtained by measuring the most prominent features in the rest-frame UV/optical spectra and applying corrections to the galaxy redshifts measured from Lyα emission lines ($z_{\rm Ly\alpha}$) and interstellar metal absorption lines ($z_{\rm IS}$). The highest precision redshifts are measured from prominent nebular emission lines with NIR spectra for which no corrections are necessary.

To reduce the systematic errors on $z_{\rm Ly\alpha}$ and $z_{\rm IS}$ we adopt the approach from Rudie et al. 2012 and Steidel et al. 2010. Using galaxies with both rest-UV and rest-optical spectosocpy, this technique calibrated the typical offset between $z_{H\alpha}$ versus $z_{\rm Ly\alpha}$ and $z_{\rm IS}$ (Steidel et al. 2010, Adelberger et al. 2005a). The following formulae presents the adopted corrections used to obtain $z_{\rm gal}$ from $z_{\rm Ly\alpha}$ (galaxies with only Lyα emission) and $z_{\rm IS}$ (galaxies with only IS absorption lines that trace the outflowing gas).

$$z_{\rm gal,IS} \equiv z_{\rm IS} + \frac{\Delta v_{\rm IS}}{c}(1+z_{\rm IS}), \tag{1.1}$$

where

$$\Delta v_{\rm IS} = 160 \quad {\rm km} \quad {\rm s}^{-1} \tag{1.2}$$

$$z_{gal,{\rm Ly\alpha}} \equiv z_{\rm Ly\alpha} + \frac{\Delta v_{\rm Ly\alpha}}{c}(1+z_{\rm Ly\alpha}), \tag{1.3}$$

where

$$\Delta v_{\rm Ly\alpha} = -300 \quad {\rm km} \quad {\rm s}^{-1} \tag{1.4}$$

For galaxies with both detected Lyα emission and IS absorption lines satisfying $z_{\rm IS} < z_{\rm gal} < z_{\rm Ly\alpha}$ we use the arithmetic mean of the values,

$$z_{\rm gal} \equiv \frac{z_{\rm Ly\alpha} + z_{\rm IS}}{2}. \quad (1.5)$$

The error for individual systemic redshift estimates are important for interpreting gas phase kinematics in C IV and Si IV. We find the rest UV redshifts exhibit 1σ scatter from the systemic velocity of $\sim$130 km s^{-1}.

Chapter 2

Methods: Absorption Line Analysis

The goal of this methods chapter is to familiarize the reader with the techniques we used to quantify C IV and Si IV absorption. This chapter will describe in detail the process of fitting the profiles of individual metal absorbers, as well as the derivation of sensitivity limits, which will be necessary for understanding plots shown in the following chapter dedicated to our results. Since we did not fit every C IV absorption system in each of the 15 QSOs, we do not have an IGM control sample to compare the C IV absorption we find associated with the presence of galaxies with "random" locations in the IGM, so we will also give an overview of the IGM control sample we used for comparisons in our results.

The positions of where C IV systems should exist (within $\pm$ 1000 km s^{-1} of the systemic redshift of each of the 711 foreground galaxies) in each 15 HIRES QSO spectra were identified automatically by python code, and if absorption was present all C IV systems were confirmed by eye. We scanned for C IV absorption doublets with a wavelength separation of $(1 + z_{gal})\delta\lambda$, where $\delta\lambda$= 2.5771 Å is the rest-frame wavelength difference between the components of the C IV $\lambda\lambda$1548, 1550 doublet. Of the 711 galaxies within $D_{tran} < 1.5$ pMpc this method found 352 galaxies whose spectra contained a C IV $\lambda\lambda$1548, 1550 doublet with 231 of those systems having an associated Si IV $\lambda\lambda$1394, 1403 doublet system. The 2D projected distance between the galaxy and the QSO line of sight (LOS) will be referred to as the galactic impact parameter, D_{tran}.

Due to the strong likelihood of finding H I associated with metal-line absorption, the validity of these C IV and Si IV systems were corroborated by the presence of H I. D'Odorico 2016 recently found that every Lyα systems with log N(HI) > 15 and 50-60% of Lyα systems with $\log(N_{HI}) > 14.5$ show associated C IV lines. While the presence of H I (seen in Lyα and Lyβ absorption) provides self-assurance in the way we were identifying our C IV and Si IV systems, it was not a requirement. As it happened, all 352 galaxies that contained C IV absorbers also had H I present (seen in Lyα absorption) at the same velocity offset.

2.1 Voigt Profile Fitting

We model the physical abundance of C IV and Si IV absorption along the QSO LOS using Voigt profiles. The Voigt profile is a normalized function that is a convolution of the Lorentzian profile from natural broadening and the gaussian profile from doppler broadening. We used Voigt profile decompositions to fit 594 unique C IV absorbers in our KBSS galaxy sample.

For the analysis of our spectra, we use the Voigt profile-fitting code VPFIT developed by Carswell and collaborators (Carswell & Webb 2014) kindly made available to us.[1] VPFIT is a χ^2 minimization program capable of simultaneously making detailed Voigt profile fits to the absorption profiles of several different transitions, for individual components of the systems, in a specified region of spectra. For each absorber, the VPFIT output file contains the redshift (z_{abs}), Doppler width (b) and column density (N_{CIV}), as well as an error estimation for each parameter. Note that we did have to provide estimates of these parameters for each C IV λ1548 and Si IV λ1394 absorber (the C IV λ1550 and Si IV λ1403 components were used in cases of contamination or saturation of the stronger component) as the initial step before we performed the Voigt profile analysis with VPFIT (Carswell & Webb 2014).

We use Voigt profiles because they give us the ability to directly measure the column density and Doppler widths of individual absorption lines, allowing us to quantify the amount of C IV and Si IV along the QSO LOS. There are also advantages to fitting C IV and Si IV doublets, in addition to doublets being relatively straight-forward to identify. Due to ionization conditions in the IGM and CGM, triply ionized C and Si are much more common than singly ionized species, i.e. their C II and Si II counterparts.

Without high resolution spectroscopy of bright quasars, it is uncommon for high redshift metal absorption line studies to posses the resolving power required to fit individual C IV doublets, as many studies are limited by the instrumental broadening function. However, the resolving power of Keck/HIRES ($R \approx 45,000$) is fully able to resolve down to a FWHM $\leqslant$ 7 km s^{-1} so that both components of the C IV and Si IV doublets are clearly defined in the QSO spectra.

An alternative approach to study absobers is the equivalent width method. Determining the equivalent width of an absorber involves decomposing the area of the absorber profile into a height, which spans from the continuum line to a flux of zero, and solving for the width (equivalent width). There is much information to be gained from knowing the intrinsic shape of the absorbers that is lost when using the equivalent width. For example, we can directly measure the column densities, i.e. the physical amount of gas along the line of sight, without needing pixel statistics.

The process of iteration involved adjusting and reevaluating Voigt profile parameters on the output file from VPFIT, as well as adding and subtracting absorption line components. Each time VPFIT's output file was edited by hand to better match the observed absorption system, it was then input to VPFIT to be rerun, this process was repeated until the VPFIT file parameters had a reduced χ^2 value which converged close to 1.0. While it was ideal to

[1] http://www.ast.cam.ac.uk/rfc/vpfit.html

have two non-contaminated components, we only need a clear profile of a single $\lambda\lambda$1548, 1550 or Si IV $\lambda\lambda$1394, 1403 system for a reliable Voigt profile fitting analysis.

Our final fits include a full Voigt profile decomposition of 594 C IV and 309 Si IV unique absorbers from the 352 galaxies with C IV and the 231 galaxies with Si IV respectively. We use the term “unique absorber" to specify that we do not assign any galaxy to a particular absorber because we do not have a complete spectroscopic galaxy redshift catalog, and we do not assign any absorber to a particular galaxy due to absorption line systems appearing in multiple galaxies around the same QSO field. For a galaxy in the same field, if their redshifts are within Δv = 1000 km s^{-1} of each other, some of the same absorption line systems will reappear regardless of the difference in impact parameter. For this reason each C IV and Si IV absorber was treated as an isolated system and each galaxy received their own particular splice of the Voigt fit spectrum.

Two examples of multicomponent C IV and Si IV absorption-line systems can be viewed in figure 2.1 below. These "stacked plots" are commonly used in the field of absorption line spectroscopy because they display multiple fits of different ion transitions being studied, in the QSO spectra surrounding the redshifts of galaxies, at once. As you see, there are successive rows corresponding to both C IV and Si IV transitions (along with the overplotted VPFIT profiles), followed by the Lyα and Lyβ transitions accompanied by their VPFIT profiles from Rudie et al. (2012). Since hydrogen is the most abundant element in the Universe, we expect H I to be present in the same gaseous halo that C IV and Si IV are found in. These plots are efficient ways to authenticate C IV and Si IV absorption line systems by eye.

2.2 The IGM Control Sample

In this work we do not assign any absorption system to a particular galaxy, rather we consider the distribution of absorbing gas within Δv = $\pm$1000 km s^{-1} of galaxies at a variety of transverse distances. In some cases we are aware of galaxies at similar redshifts lying closer to the QSO line of sight, while at the same time we are unaware of the locations of every galaxy in our surveyed volume due to the incompleteness of our spectroscopic galaxy redshift catalog compared to our photometrically selected sample. Since we are looking at galaxies distributed in a cosmological volume and we don't know the redshifts of every galaxy within that volume, we can't ascertain which galaxies are actually associated with which absorbers, so we always plot the distributions for all galaxies to study absorption in a statistical manner.

Lacking the ability to associate individual galaxies and absorbers, if we want to quantify the enhancement of CIV and Si IV metal absorption around galaxies, we can compare our observed distributions to equivalent measurements made towards random locations in the Universe. This can be done by using a control sample of absorption systems towards QSO lines of sights that is independent of the positions of foreground galaxies. We use the Boksenberg & Sargent catalog to understand the C IV and Si IV distribution at random locations in the IGM, which will now be referred to as the BXS15 catalog for data comparison.

Boksenberg & Sargent applied Voigt-profile-fitting procedures to Keck HIRES spectra of

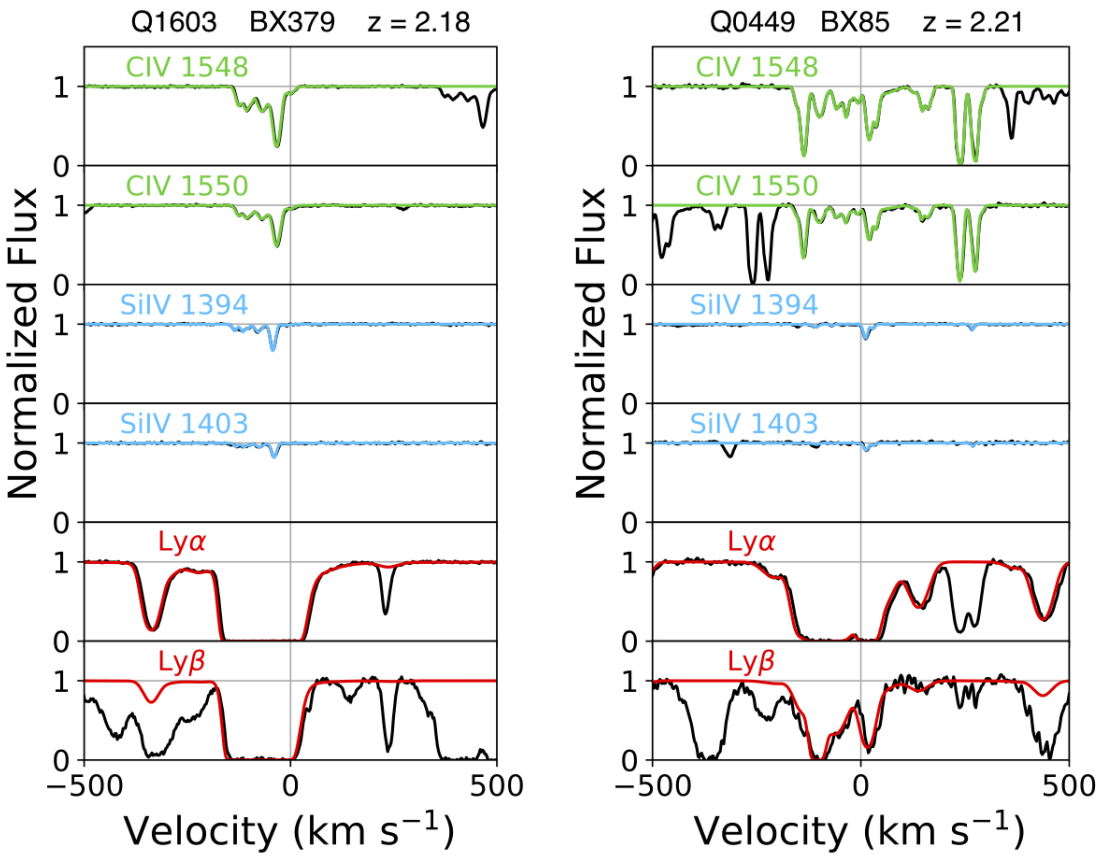

Figure 2.1: Example fits to the KBSS QSO data surrounding a galaxy with a large multi-component absorption-line system. Displayed in black are the continuum-normalized HIRES spectra of the C IV $\lambda\lambda$1548, 1550 and Si IV $\lambda\lambda$1394, 1403 with additional Lyα and Lyβ transitions (provided from the H I fits in Rudie et al. 2012) within $\pm$500 km s^{-1} of the system redshift of the indicated galaxy. Overplotted in color are the Voigt profile decompositions within $\pm$500 km s^{-1} of the galaxy.

six QSOs and produced an absorber catalog composed of 346 C IV absorber components within the redshift range of interest for the KBSS survey. BXS15 began identifying metal absorption line systems by the presence of C IV measurements made mostly outside of the Lyα forest. C IV was the only ion detected in the weakest systems. With the BXS15 sample carefully scanning for C IV, using the same chi-squared minimization technique VPFIT (described above), and having a subset of background QSOs that fell within the same high redshift range as our KBSS sample, BXS15 is an ideal comparison sample.

In order to compare our resulting covering fractions and C IV kinematics with the IGM sample, we measured the same statistics for each catalog. This distribution was obtained by drawing each QSO from the BXS15 catalog and pairing it with every KBSS galaxy redshift and impact parameter. QSO: Q1442+2931, was the only QSO to overlap between both catalogs, so we made sure to only use five BXS15 QSOs (excluding Q1442+2931) to randomly draw a QSO and impact parameter (from our impact parameter list) to the QSO sight-line.

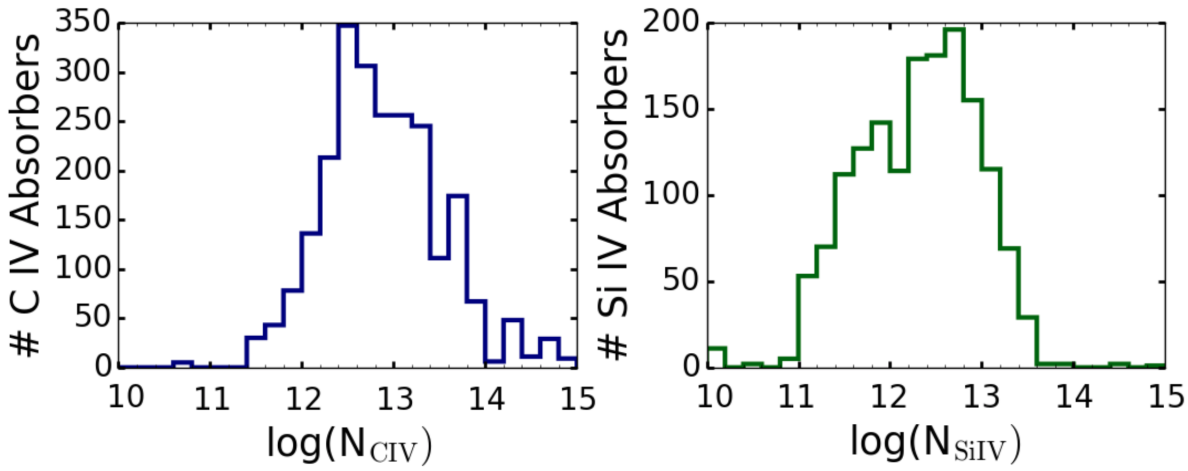

Figure 2.2: Histograms for all C IV column densities (left panels) and Si IV column densities (right panels), this is for all detected absorption line components in the KBSS sample.

Once the redshifts representing the exact distribution of our KBSS galaxies, and transverse distance to the QSO line of sight were chosen we computed the covering fraction and total summed column density from the C IV absorber parameters in the BXS15 catalog (sum(N_{CIV}) and sum(N_{SiIV})). Not only does this measurement provide quantitative data showing the distribution of C IV around random locations, but it provides insight into whether or not the gas surrounding galaxies has excess C IV and Si IV absorption compared with a random location.

While we did not put a column density cutoff when building our catalog of absorbers, Boksenberg and Sargent used a threshold of $N_{CIV} > 10^{12.5}$ cm^{-2} for their C IV absorbers and $N_{SiIV} > 10^{11.8}$ cm^{-2} for their Si IV absorbers. Therefore for comparison purposes our plots are made to show sensitivity to all C IV and Si IV absorbers using the BXS15 C IV and Si IV column density cuts as an acceptance threshold.

2.3 Computing Density Sensitivity Limits

In Chapter 3 we will present the results of this work and discuss the total integrated amounts of C IV and Si IV detected along the line of sight for individual galaxies. As we will see, with the high resolution of the KBSS QSO spectra we are able to successfully detect, resolve, and fit systems with low column densities. However, we must be able to quantify the significance of C IV and Si IV gas enhancement in galaxies with weakly or undetected absorption− we need to find the limiting column densities for those galaxies. This limiting column density is essentially the column density that an absorber would need to have in order to be detected in a velocity window around the redshift of a galaxy given contamination and noise. Our goal was to find the most stringent limit possible so that it properly addressed complications from the data such as: noise in the spectra, self-contamination from C IV and unidentified IGM contamination.

A great benefit of using C IV for Voigt profile fitting, is that if at least one of the C IV$\lambda\lambda$1548, 1550 doublet is free from contamination and saturation, we can still successfully fit the C IV system, the same is true of the Si IV $\lambda\lambda$1394, 1403 doublet. This means that since we are dealing with doublets, when we determine the limiting column density for C IV, we will look at two sections of QSO spectra in order to fully quantify the effect that contamination has on our ability to measure the column density.

To calculate the minimum column density a C IV absorber would need to have to be detected around a galaxy in one of the 15 QSO spectra. We start by taking the section of QSO spectra which correspond to $\pm$ 350 km s^{-1} and $\pm$ 700 km s^{-1} velocity windows centered around the systemic redshift of each galaxy (we will motivate the width of these adopted windows in the following chapter). We also look into the error spectra (the error calculated from flux value in the QSO continuum normalized spectra) to provide us with the most robust limiting column density. The limiting equivalent width from the noise spectrum (σ_W) is the minimum amount of absorption that could exist in the spectrum and be undetectable because of noise in the spectrum. Whereas the limiting equivalent width from the flux spectrum (W(v)) is the minimum amount of absorption that could exist in the spectrum and be undetectable due to contamination.

We began this process by interpolating the, F_λ, spectrum and error spectrum, σ_F, of C IV and Si IV for both doublet transitions onto a velocity scale via Equations 2.1 – 2.3.

$$\frac{\Delta v}{c} = \frac{\Delta \lambda}{\lambda} = \frac{\lambda_r - \lambda_o}{\lambda_o} \tag{2.1}$$

$$\Delta v_{\mathrm{CIV\_1548}} = \frac{\lambda_r - \lambda_{\mathrm{CIV\_1548}}}{\lambda_{\mathrm{CIV\_1548}}} \cdot c, \quad \Delta v_{\mathrm{CIV\_1550}} = \frac{\lambda_r - \lambda_{\mathrm{CIV\_1550}}}{\lambda_{\mathrm{CIV\_1550}}} \cdot c \tag{2.2}$$

$$\Delta v_{\mathrm{SiIV\_1394}} = \frac{\lambda_r - \lambda_{\mathrm{SiIV\_1394}}}{\lambda_{\mathrm{SiIV\_1394}}} \cdot c, \quad \Delta v_{\mathrm{SiIV\_1403}} = \frac{\lambda_r - \lambda_{\mathrm{SiIV\_1403}}}{\lambda_{\mathrm{SiIV\_1403}}} \cdot c \tag{2.3}$$

, where c is the speed of light in km s^{-1}, λ_r is the rest-wavelength array (from one of the 15 KBSS QSOs) surrounding the systemic redshift of the galaxy, and λ_o is the rest-frame wavelength for the C IV and Si IV doublet transitions.

Next, we calculate the implied equivalent width for each pixel in the spectrum as shown in Equation 2.4, and we calculate the equivalent width from the error spectrum as shown in 2.5, where $\Delta\lambda$(v) for both equations is the pixel sampling sampling in velocity space in angstroms.

$$\mathrm{W\,(v)} = (1 - F_\lambda)\,\Delta\lambda(\mathrm{v}) \tag{2.4}$$

$$\sigma_W(\mathrm{v}) = \sigma_F * \Delta\lambda(\mathrm{v}) \tag{2.5}$$

We take the first pixel in W(v) and compare it to the first pixel in σ_W(v) to see if the equivalent width in the W(v) pixel is significant enough to formally be considered a detection,

this process is iterated through each pixel. In cases where $\mathrm{W(v)} > 2\sigma_W(\mathrm{v})$, we consider the data to be consistent with the pixel containing real absorption (either contamination or due to true metallic absorption of interest). Since the C IV and Si IV doublets each have two transitions, when $\mathrm{W(v)} < 2\sigma_W(\mathrm{v})$ (i.e. when the data is consistent with a non-detection) we take the pixel value of the limiting equivalent width from the stronger of the two ionic transitions to give a better constraint on the limiting column density.

When significant absorption is detected we use the pixel from the transition with the lowest level of absorption to minimize the effect of contamination and ensure we are calculating the most sensitive limit allowed by the data. To do so, we compare the equivalent width at each pixel in each of the two transitions normalized by the transitions sensitivity, using the atomic parameters.

For each transition we transform each equivalent width pixel into an $\alpha(\mathrm{v})$ pixel, which is normalized by the transition sensitivity and is therefore proportional to the column density in the non-saturated regime. The first value in the α and the first value in the σ_α were compared to see which one had the higher sensitivity to absorption, this was continued for the values each consecutive position. This was done for both Si IV and C IV ions at each given position in the QSO spectrum and error spectrum to ensure we had the less contaminated spectrum from each transition. In other words for non-detections we always derive the limiting equivalent width from the stronger transition (the 1548 transition in the case of C IV and 1394 for Si IV), but for detections we check which of the two doublet transitions had a less contaminated spectrum.

$$\alpha_{\mathrm{CIV}}\left(\mathrm{v}\right) = \begin{cases} \dfrac{\mathrm{W}_{0,1548}\left(\mathrm{v}\right)}{{\lambda_{\mathrm{e},1548}}^2 \cdot \Gamma_{1548}} & \text{if} \quad \mathrm{W}_{1548}(\mathrm{v}) < 2\sigma_{\mathrm{W}_{1548}}(\mathrm{v}) \\ \min\left[\dfrac{\mathrm{W}_{0,1548}\left(\mathrm{v}\right)}{{\lambda_{\mathrm{e},1548}}^2 \cdot \Gamma_{1548}}, \dfrac{\mathrm{W}_{0,1550}\left(\mathrm{v}\right)}{{\lambda_{\mathrm{e},1550}}^2 \cdot \quad \Gamma_{1550}}\right] & \text{if} \quad \mathrm{W}_{1548}(\mathrm{v}) > 2\sigma_{\mathrm{W}_{1548}}(\mathrm{v}) \end{cases} \tag{2.6}$$

$$\sigma_{\alpha_{\mathrm{CIV}}}\left(\mathrm{v}\right) = \begin{cases} \dfrac{\sigma_{\mathrm{W}_{1548}}\left(\mathrm{v}\right)}{{\lambda_{\mathrm{e},1548}}^2 \cdot \Gamma_{1548}} & \text{if} \quad \mathrm{W}_{1548}(\mathrm{v}) < 2\sigma_{\mathrm{W}_{1548}}(\mathrm{v}) \end{cases} \tag{2.7}$$

The α values contain information on the limiting column density at each velocity offset along the spectrum. In our work we will also be presenting results for the sum of the column density, integrated over all the absorption across a velocity window centered on the redshift of individual galaxies. We now describe how we use $\alpha(\mathrm{V})$ values to compute the errors and limits on these summed column densities. We take the sum of the spectrum α and the quadratic sum of the the error spectrum σ_α for both C IV and Si IV. We then finished converting into a column densities using equation 2.8 which assumes a linear curve-of-growth regime (optically thin regime, where the number of absorbing atoms is proportional to equivalent width of the line). For each ion we compute two quantities: the limiting summed column density computed from integrating α (N_α), and the limiting summed column density as computed from integrating the σ_α arrays.

$$\mathrm{N} \quad = \quad 4\pi\varepsilon_0 \frac{m_\mathrm{e} c^2}{\pi \mathrm{e}^2}(\mathrm{W}) \quad \mathrm{cm}^{-2} = 1.13\mathrm{E}20 \times \alpha \quad \mathrm{cm}^{-2} \tag{2.8}$$

, where $\mathrm{m_e}$ = 9.11E-28 g, c = 2.998E+10 cm s^{-1}, e = 4.81E-10 esu.

$$\mathrm{N}_{\alpha_{\mathrm{CIV}}} \quad = \quad 1.13\mathrm{E}20 \quad \times \quad \sum \alpha_{\mathrm{CIV}} \cdot \mathrm{cm}^{-2} \tag{2.9}$$

$$\sigma_{\mathrm{N_{CIV}}} \quad = \quad 1.13\mathrm{E}20 \quad \times \quad \sqrt{\sum {\sigma_{\alpha_{\mathrm{CIV}}}}^2} \cdot \mathrm{cm}^{-2} \tag{2.10}$$

$$\mathrm{N}_{\alpha_{\mathrm{SiIV}}} \quad = \quad 1.13\mathrm{E}20 \quad \times \quad \sum \alpha_{\mathrm{SiIV}} \cdot \mathrm{cm}^{-2} \tag{2.11}$$

$$\sigma_{\mathrm{N_{SiIV}}} \quad = \quad 1.13\mathrm{E}20 \quad \times \quad \sqrt{\sum {\sigma_{\alpha_{\mathrm{SiIV}}}}^2} \cdot \mathrm{cm}^{-2} \tag{2.12}$$

Lastly, we decided between using N_α and σ_N for the upper limits on the sum($\mathrm{N_{CIV}}$) and sum($\mathrm{N_{SiIV}}$) statistics. Once the log column density and the error were calculated in Equations 2.9 – 2.12, we took the maximum value between N_α and $2\sigma_N$ to be the upper limit on a KBSS galaxy's minimally detectable summed column density. The former being taken in the case of significant contamination, and the later in the case that the noise in the observed spectrum sets the level of detectable absorption. In order to check the reliability of this calculation, we also calculated the limits based off each transition individually, i.e. $\alpha_{\mathrm{CIV1548}}$ and $\sigma_{\alpha_{\mathrm{CIV1548}}}$. These were compared to our result in Equations 2.13 and 2.14 to verify that we produced a more conservative limit.

$$\mathrm{N_{CIV}(limit)} \quad = \quad \max[\mathrm{N}_{\alpha\_\mathrm{CIV}}, 2\sigma_{\mathrm{N_{CIV}}}] \quad \mathrm{cm}^{-2} \tag{2.13}$$

$$\mathrm{N_{SiIV}(limit)} \quad = \quad \max[\mathrm{N}_{\alpha\_\mathrm{SiIV}}, 2\sigma_{\mathrm{N_{SiIV}}}] \quad \mathrm{cm}^{-2} \tag{2.14}$$

In the next chapter we will discuss how Voigt profile fitting, upper limits on the C IV and Si IV column densities, and the BXS15 sample were used to further our understanding of gas in the CGM. The results chapter will focus on the spatial and kinematic distribution of metal absorption in the CGM of galaxies. Throughout the chapter the BXS15 sample will provide typical IGM column densities for C IV and Si IV to properly evaluate the significance of the enhanced metal absorption we find.

Chapter 3

Results: The Size Scale and Kinematics of the Metal-Enriched CGM

We begin the results chapter by discussing the distributions of C IV and Si IV absorbers as a function of velocity and impact parameter to further our understanding of gas in the CGM. Through the use of covering fractions and sum statistics we show strong correlations between the physical amount of metal-bearing gas with an increasing proximity to galaxies. We also observe that the frequency with which we observe C IV and Si IV absorbers increases dramatically as we approach the CGMs of these star-forming galaxies. The C IV and Si IV gas statistics used in this work are compared to the typical absorption at random locations in the IGM using the BXS15 catalog, in order to quantify the significance of C IV and Si IV gas enhancement out to 1.5 pMpc from high-z, star-forming galaxies.

3.1 Velocity-Space Distributions

One way that we are able to measure properties of C IV and Si IV bearing gas near galaxies, is to look at the velocity of C IV and Si IV absorbers compared to the systemic velocities of galaxies. We achieve this by measuring velocity-space distributions from C IV and Si IV and comparing to the H I distribution measured in Rudie et al. 2012, as seen in Figure 3.1. We compute the velocity distribution on two difference spatial scales to show the velocity distribution of all C IV and Si IV absorbers. In Figure 3.1 we use $N_{CIV} > 10^{12.5}$ cm^{-2}, $N_{SiIV} > 10^{11.8}$ cm^{-2} (limiting column density for Si IV from BXS15) and $N_{HI} > 10^{14.5}$ cm^{-2} (H I absorbers above this threshold have been found to be tightly correlated with the positions of galaxies Rudie et al. 2012) within 100 pkpc (left panels) and 300 pkpc (right panels) from the QSO line of sight. $D_{Tran} < 100$ pkpc was chosen because the typical virial radius for a KBSS galaxy is $\sim$90 pkpc, given the typical halo mass and redshift of the sample. $D_{Tran} <$ 300 pkpc was chosen because it was found to be the defining bounds of the CGM as traced in H I (Rudie et al. 2012). We define the velocity offset (Δv) of an absorber as:

$$\Delta \mathrm{v} \equiv \frac{(z_{abs} - z_{gal})c}{1 + z_{gal}} \tag{3.1}$$

where z_{abs} is the redshift of the absorber, c is the speed of light, and z_{gal} is the systemic redshift of the galaxy described in Chapter 1. Therefore a negative velocity indicates an absorber is blueshifted compared to z_{gal}.

The measured velocity dispersion within $\mathrm{D_{Tran}} < 100$ pkpc is 256 $\pm$ 30 km s^{-1} for C IV and is 211 $\pm$ 24 km s^{-1} for Si IV. As we move away from the KBSS galaxies, the velocity dispersion of absorbers decreases for both ions. The bulk of C IV and Si IV absorbers is concentrated around $\Delta v = 0$ for our set of star forming galaxies. We included the maximum velocity absorber ($\mathrm{V_{MAX}}$) for C IV and Si IV at $\mathrm{D_{Tran}} < 100$ pkpc to highlight the full velocity extent of metal bearing absorbers within the virial radius.

The velocity dispersion for C IV at $\mathrm{D_{Tran}} < 300$ pkpc is 175 km s^{-1}, we adopt the 2σ width of this distribution (i.e. 350 km s^{-1}) as a velocity cut for many of the upcoming plots in the following work. However, that value excludes some of the absorbers associated with our KBSS galaxies. If we look at the distribution of absorbers within 100 pkpc (approximately the virial radius of these galaxies) then we see that the full envelope of their distribution goes out to 700 km s^{-1}, and so we also present plots which account for all absorbers within 700 km s^{-1}. While using this extended window may include contaminating absorbers for galaxy spectra at large impact parameters, it definitely includes all the absorbers that we detect.

Now that we have looked at the C IV and Si IV absorbers velocity dispersions (in Figure 3.1), we will look at scatter plots of the absorber velocities as a function of $\mathrm{D_{Tran}}$ (in Figure 3.2). On this figure we also overplot the escape velocity thresholds for 3 different halo masses [$10^{11.7}$, $10^{11.9}$, $10^{12.1}$]. Note that the absorber velocities we measure are a lower limit on their 3D velocity since we can only measure their line of sight velocity and have no constraint on their tangential velocity.

To calculate the escape velocity threshold, we assume the galaxies live in dark matter halos that follow a Navarro-Frenk-White (NFW 1997) density profile with a concentration (c=3) following Duffy et al (2008). Under this assumption we are able to calculate the escape velocity as a function of radius, and see how much metal enriched gas is moving at a high enough velocity to escape the halos. We find some C IV and Si IV absorbers within 100 pkpc in excess of the escape velocity. In the next section we will show that within this distance we observe roughly a factor of 9 enhancement for C IV (factor of 5 for Si IV) enhancement in the absorber covering fraction with respect to random lines of sight, making it highly probable that these high velocity absorbers correspond to unbound gas associated with, and likely ejected from the halos of galaxies

While we can't say whether or not that particular gas is associated with the KBSS galaxy we are looking at, or if it's random absorption along the line of sight, we can use the escape velocity curves to see the scale on which C IV and Si IV absorbers correspond to unbound gas. Also, since we do not have 3D velocities for these absorbers and are looking at the line of sight projection of the velocity vector, we cannot claim that the gas from the C IV and Si IV absorbers that falls within the escape velocity bounds are bounded to that galaxy.

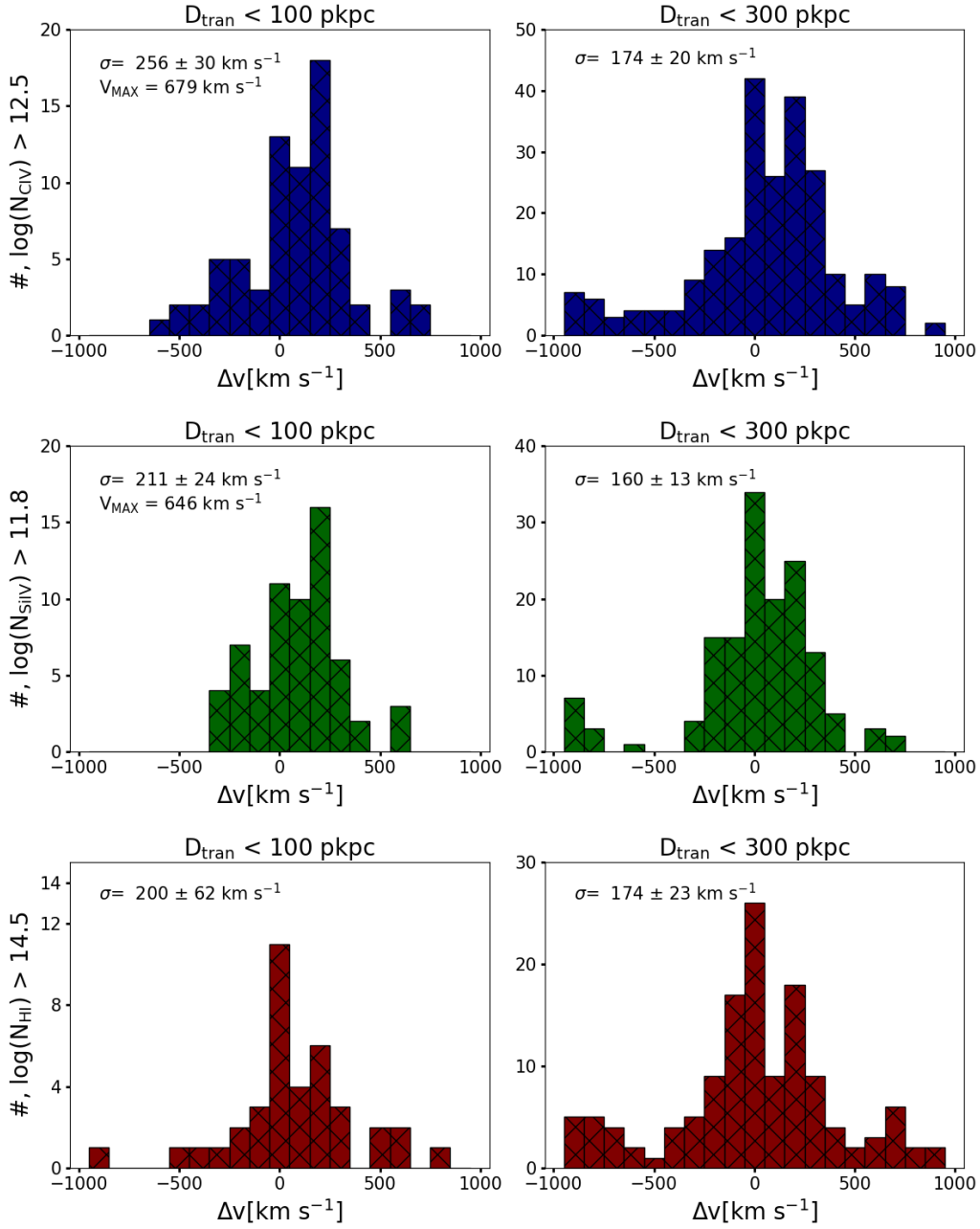

Figure 3.1: The velocity-space distribution of the number of $N_{CIV} > 10^{12.5}$ cm^{-2}, $N_{SiIV} > 10^{11.8}$ cm^{-2} and $N_{HI} > 10^{14.5}$ cm^{-2} absorbers within 100 pkpc (left panel) and 300 pkpc (right panel) from the line of sight. The H I absorber distributions from Rudie et al. (2012) have been included to show comparisons between the three different ion absorptions of the same KBSS catalog. The 6 panels also include the velocity dispersion σ of the distributions and the maximum velocity V_{MAX} of an absorber within $D_{Tran} < 100$ pkpc for C IV and Si IV. The centroid of the highest velocity absorber within $D_{Tran} < 100$ pkpc that has $N_{CIV} > 10^{12.5}$ cm^{-2} is 680 km s^{-1} in C IV and 646 km s^{-1} in Si IV.

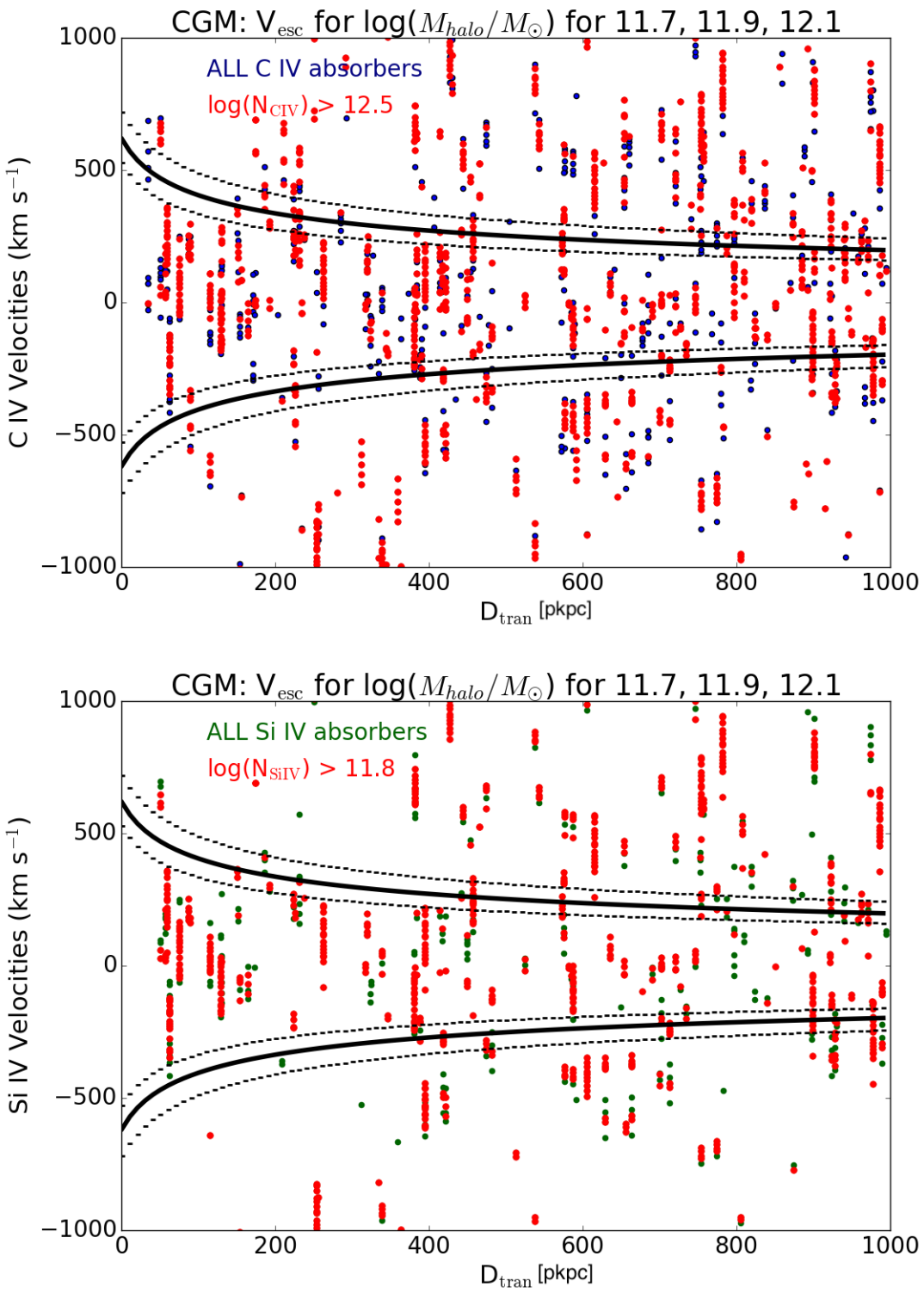

Figure 3.2: Scatter plots of the velocities for C IV (top plot) absorbers and Si IV (bottom plot) absorbers as a function of D_{Tran} (pkpc), with escape velocity thresholds for 3 different halo masses. Dotted and solid lines are drawn on the plots to indicate the escape velocities of absorbers as a function of radius for three different halo masses, log(M) = [11.7,11.9,12.1].

3.2 C IV and Si IV Spatial Distributions

We have seen how the frequency of C IV and Si IV absorbers is correlated with the absorber's relative velocity from the systemic redshift of the host galaxy. Now we will consider how C IV and Si IV absorbers are distributed in the plane of the sky. First, we consider covering fraction of absorbers as a function of D_{tran} to quantify the likelihood of detecting C IV and Si IV of a given column density as we approach a galaxy.

We evaluated our covering fraction statistics as the quantity of galaxies where C IV and Si IV systems were detected over the number of galaxies where C IV and Si IV could have been detected. The areas of the QSO spectra, within $\Delta v = 1000$ km s^{-1} of the galaxy redshift, where there existed too much IGM absorption to properly identify C IV and Si IV absorption features, were omitted from our statistics.

Figures 3.3 and 3.4 shows the covering fractions of C IV and Si IV absorbers within 1.5 pMpc of galaxies using two velocity cuts as described in Section 3.0.1. All four panels are plotted in impact parameter bin sizes of 100 pkpc, which corresponds to roughly the virial radius of these galaxies. Notice the highest covering fraction one can get is 1.0, because at this point 100 % of the galaxies within a given impact parameter bin have sufficiently strong absorption. When comparing the covering fraction (f_c) of C IV absorbers within $\pm$350 km s^{-1} to C IV absorbers within $\pm$700 km s^{-1}, we see an equal, high covering fraction at impact parameters $<$ 100 pkpc. The same finding of equally high covering fractions for absorbers within both velocity cuts, within $<$ 100 pkpc, is seen for Si IV absorbers.

As impact parameter increases for each of the 4 plots in Figures 3.3 and 3.4, f_c decreases for both C IV and Si IV. While the f_c for Si IV absorbers is lower at all impact parameters than C IV, the overall shape of the Si IV f_c distribution is similar to that of C IV. The enhancement of C IV above the level at which the distribution plateaus extends to 400 pkpc (more prevalent within $\pm$700 km s^{-1}) while the Si IV enhancement extends to 200 pkpc, before the covering fraction levels out. While the prominent abundance of C IV in the CGM sample does level out around 400 pkpc, we see a significant enhancement of C IV absorption in comparison to the BXS15 absorption all the way out to 1.5 pMpc. The same is true for the Si IV distribution, but after 200 pkpc. We discuss the physical interpretation of this enhancement in the Conclusions chapter.

We measured the sum(N_{CIV}) and sum(N_{SiIV}) (the log of the sum of the N_{CIV} and N_{SiIV} of all the absorbers within the given velocity bin) in Figures 3.7 and 3.8 to show the relationship of increasing column density with decreasing galactic impact parameter. The sum is computed by adding the column densities of each VPFIT decomposed absorption line system associated within $\pm$ 350 km s^{-1} or $\pm$ 700 km s^{-1} of the systemic galaxy redshift. See equation 3.2 for how we computed the error propagation for this sum (done in log-space) from the output column density uncertainties from VPFIT.

$$\sigma_{\log_{10}(N)} = \frac{\sqrt{(\sigma_{\log_{10}(N_a)} \cdot \log_{10}(N_a))^2 + (\sigma_{\log_{10}(N_b)} \cdot \log_{10}(N_b))^2 + ... + (\sigma_{\log_{10}(N_n)} \cdot \log_{10}(N_n))^2}}{\log_{10}(N_a) \quad + \quad \log_{10}(N_b) \quad + ... + \quad \log_{10}(N_n)} \tag{3.2}$$

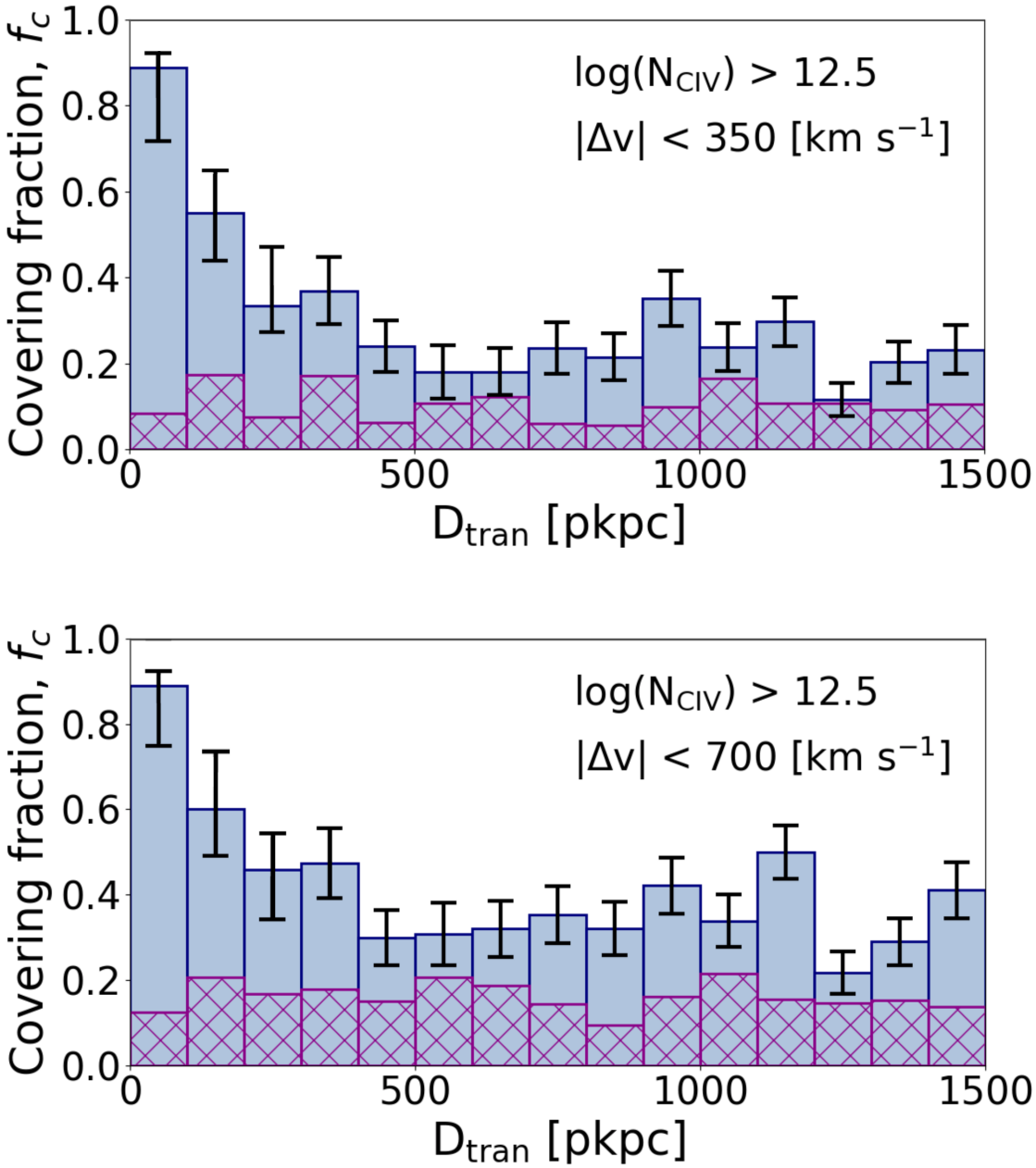

Figure 3.3: The covering fraction, f_c, of absorbers for thresholds of $\log(N_{CIV}) = 12.5$ as a function of D_{tran}. The first C IV plot takes into account C IV absorbers that fall within $\pm$350 km s^{-1} of the system redshift of the galaxy, while the second plot uses absorbers that fall within $\pm$700 km s^{-1} of the systemic redshift. The solid histogram represents the covering fraction of C IV absorbers from our KBSS CGM sample, while the hatched histogram represents f_c at random locations in the IGM taken from BXS15. For when the number of galaxies in a given bin size was <20, the error bars were calculated from a binomial distribution, otherwise we assumed a Gaussian distribution. Both plots are plotted in impact parameter bin sizes of 100 pkpc.

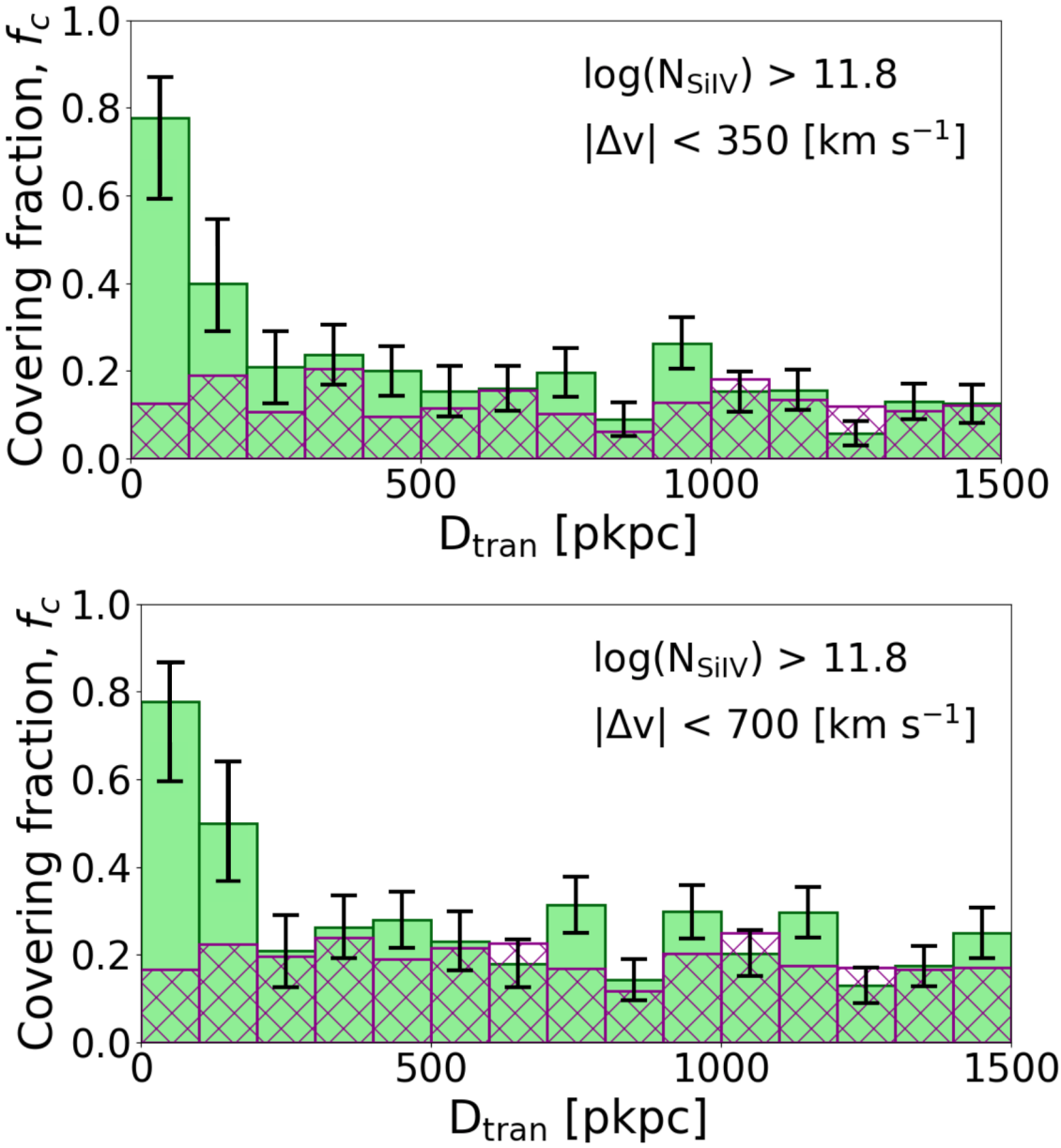

Figure 3.4: The covering fraction, f_c, of absorbers for thresholds of $\log(N_{SiIV}) = 11.8$ as a function of D_{tran}. The first Si IV plot takes into account Si IV absorbers that fall within ± 350 km s^{-1} of the system redshift of the galaxy, while the second plot uses Si IV absorbers that fall within ± 700 km s^{-1} of the systemic redshift. The solid histogram represents the covering fraction of Si IV absorbers from our KBSS CGM sample, while the hatched histogram represents f_c at random locations in the IGM taken from BXS15. For when the number of galaxies in a given bin size was <20, the error bars were calculated from a binomial distribution, otherwise we assumed a Gaussian distribution. Both plots are plotted in impact parameter bin sizes of 100 pkpc.

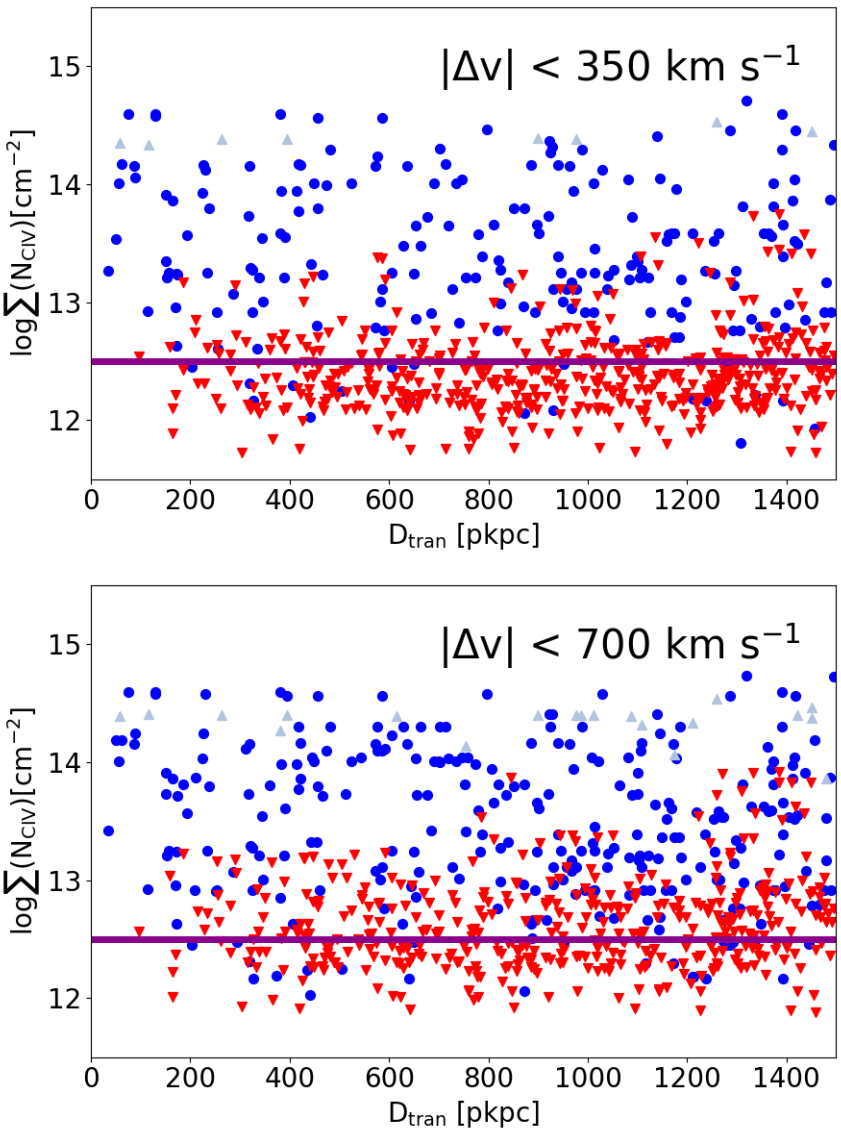

Figure 3.5: The two figures above are scatter plots, where each marker represents the total summed column densities of C IV for each of the 711 galaxies in the KBSS sample, as a function of impact parameter. Detections are indicated with blue circles for C IV, with non-detections represented by downward facing red triangles with column densities corresponding to upper limits, and with lower limits values represented by light blue upward triangles. Each of the plots either has a velocity cut of absorbers to be within $\pm$350 km s^{-1} of the system redshift of the galaxy or within $\pm$700 km s^{-1}. The purple horizontal line represents the BXS15 completeness limit at $\log(N_{CIV}) = 12.5$

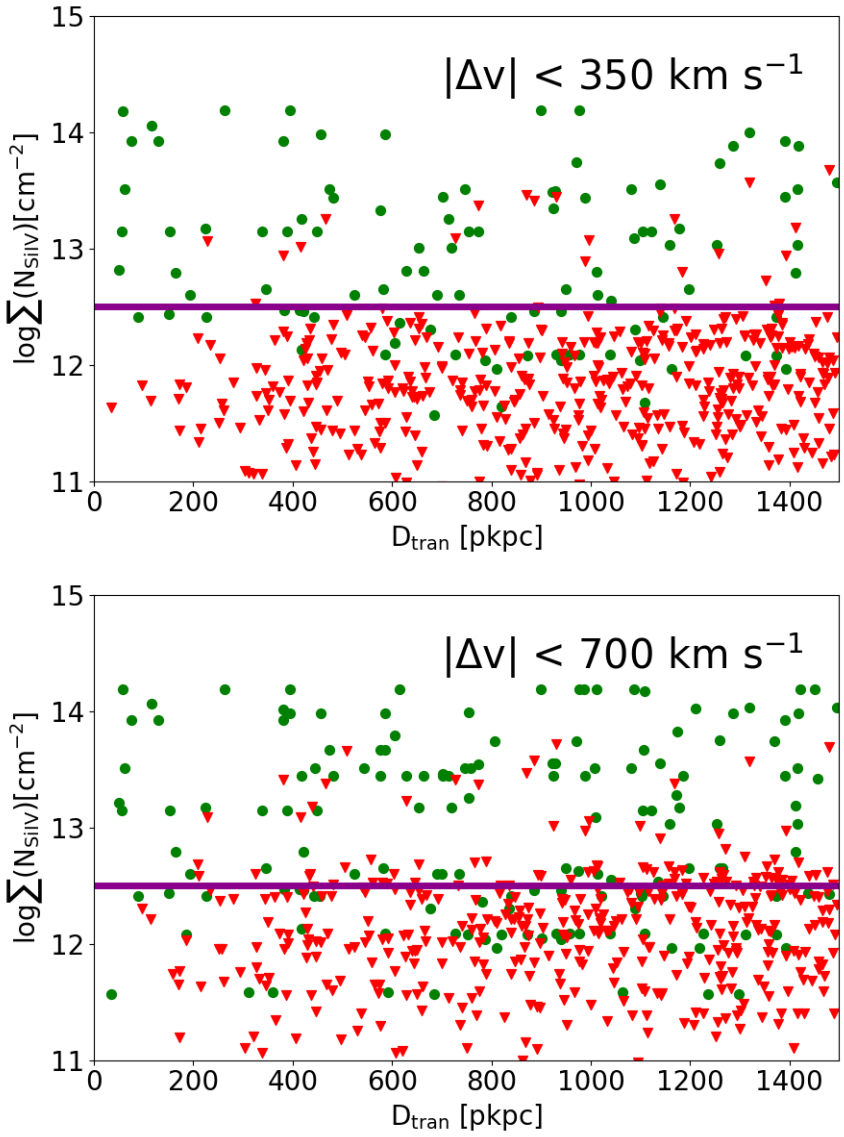

Figure 3.6: The two figures above are scatter plots, where each marker represents the total column densities of Si IV for each of the 711 galaxies in the KBSS sample, as a function of impact parameter. Detections are indicated with green circles for Si IV, with non-detections represented by downward facing red triangles with column densities corresponding to upper limits. Each of the figures either has a velocity cut of absorbers to be within $\pm$350 km s^{-1} of the system redshift of the galaxy or within $\pm$700 km s^{-1}. The purple horizontal line represents the BXS15 completeness limit at $\log(N_{SiIV}) = 11.8$.

, where N is the column density obtained from VPFIT and the individual absorption line components are represented by subscripts (a,b,..n).

While the recovery region of C IV $\lambda\lambda$1548, 1550 lies well outside the Lyα forest, λ <1216(1 + z_{QSO}) Å, Si IV $\lambda\lambda$1394, 1403 is in closer proximity to the edge of the forest and is therefore more likely to experience contamination from H I. For the Si IV plots in Figures 3.6 and 3.8, we exclude the 134 KBSS galaxies that had a redshift where Si IV fell within the Lyα forest− in order to clean contaminated Si IV absorbers. The criteria for this redshift cut is shown in equation 3.3. We will now move into looking at the scatter plots of the total N_{CIV} and N_{SiIV} per galaxy as a function of D_{tran}.

$$1 + z_{gal} > \frac{(1 + z_{QSO}) \cdot \lambda_{e,1216}}{\lambda_{e,1394}} \tag{3.3}$$

The plots in Figures 3.5 and 3.6 that can be used to get a sense of the amount of C IV and Si IV that was detected per galaxy, as well as the contamination present within the $\pm$350 km s^{-1} and $\pm$700 km s^{-1} windows of the 15 QSO spectra. The downward red triangles represent upper limits, and those limits are chosen from one of two methods demonstrated in Equations 2.2 and 2.3. A detection can also become a lightly filled in upward facing triangle (blue for C IV and green for Si IV) to represent a lower limit, which occurs if the column density obtained from VPFIT was from a system in which both C IV doublet components were saturated (Si IV is never saturated in our data). The purple horizontal line represents the BXS15 completeness limit at $\log(N_{CIV}) = 12.5$ in Figure 3.7 and $\log(N_{SiIV}) = 11.8$ in Figure 3.8.

In Chapter 2 we discussed the calculation of the most sensitive upper limits allowed by the data. The reason we wanted these upper limits to be very conservative was so when these figures show a red upside down triangle, we are confident that if a C IV of Si IV system was present in that slice of QSO spectra it would have been found if its total column density was above that limit. Again, a complete description on the limit determination process was provided in the subsection: Computing Limiting Column Densities in Chapter 2.

Figures 3.6,3.5, 3.7 and 3.8 show the statistics for Σ(N) in bins of impact parameter at the median transverse distance D_{tran}. This statistic traces the enhanced amount of C IV and Si IV absorption within the circumgalactic medium of KBSS galaxies.

These sum statistics represent the spatial distribution of the total summed column densities for N_{CIV} and N_{SiIV} as a function of transverse distance D_{tran}. Figures 3.7 and 3.8 are a way to interpret the total integrated N_{CIV} and N_{SiIV} along the QSO line of sight. Similar to the scatter plots, we consider C IV and Si IV absorbers within $|\Delta v| < 350$ km s^{-1} and $|\Delta v| < 700$ km s^{-1} windows of the systemic redshift of the galaxies.

The median, 75th and 25th percentile values for $\log_{10}(\Sigma(N))$ are displayed as a circle (blue for C IV and green for Si IV), with the median circle appearing with twice the radius. When more than 25%, 50% or 75% of the galaxies have no detected C IV or Si IV absorption, the corresponding circle is then represented by a downward triangle (indicating the limiting total column density). The black vertical bars span the 75th−25th percentile range of the

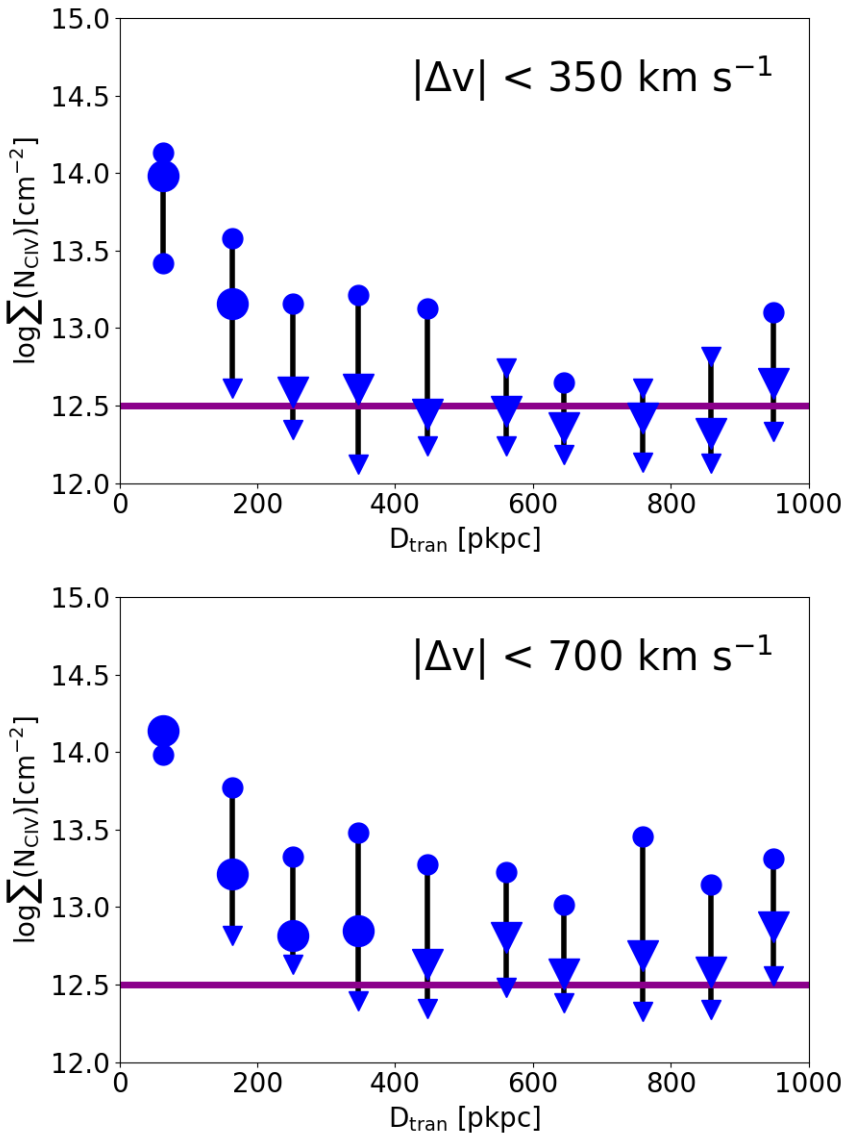

Figure 3.7: The log column densities of the sum of N_{CIV} absorbers as a function of transverse distance. We consider the $\Sigma(N_{CIV})$ statistic shown in Figure 3.3, the log of the sum of the absorbers within $|v| < 350$ km s^{-1} and $|v| < 700$ km s^{-1} of the systemic redshift of the galaxies. The median, 75th and 25th percentile values for log(SUM(N)) are displayed as a circle, with the median circle appearing twice the size. When more than 25%, 50%, or 75% of the galaxies in a given bin have more limits than detections, the corresponding circle becomes a downward facing triangle. The horizontal purple lines represent the BXS15 sample and the black vertical bars span the 75th-25th percentile range of the dispersions and are centered on the median D_{tran} of the galaxies within the given 100 pkpc bin.

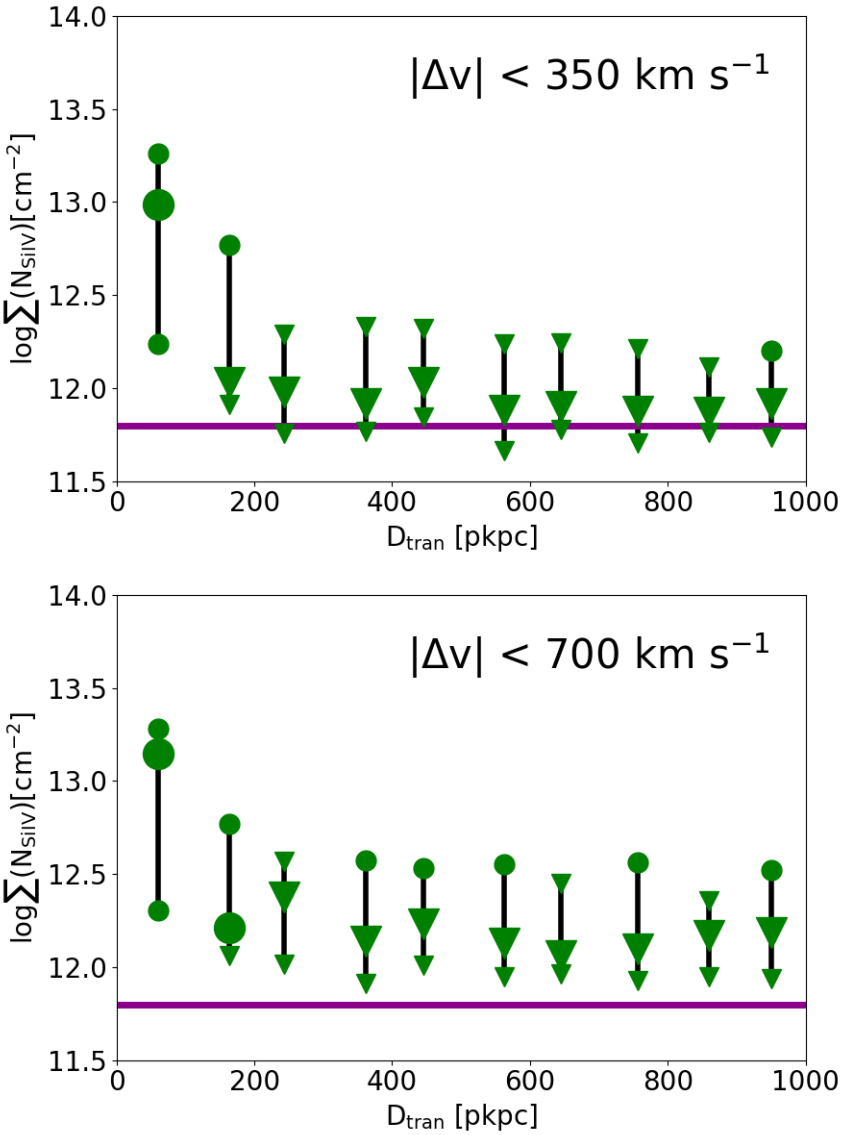

Figure 3.8: The log column densities of the sum of N_{SiIV} absorbers as a function of transverse distance. We consider the $\Sigma(N_{SiIV})$ statistic shown in Figure 3.4, the log of the sum of the absorbers within $|\Delta v| < 350$ km s^{-1} and $|\Delta v| < 700$ km s^{-1} of the systemic redshift of the galaxies. The median, 75th and 25th percentile values for $\log_{10}(\Sigma(N))$ are displayed as a circle, with the median circle appearing twice the size. When more than 25%, 50%, or 75% of the galaxies in a given bin have more limits than detections, the corresponding circle becomes a downward facing triangle. The horizontal purple lines represent the BXS15 sample and the black vertical bars span the 75th-25th percentile range of the dispersions and are centered on the median D_{tran} of the galaxies within the given 100 pkpc bin.

dispersions and are centered on the median D_{tran} of the galaxies within the given 100 pkpc bin.

Since we use such stringent upper limits, we can make claims from these plots based on the absorber detections. The main difference we see between the ± 350 km s^{-1} and ± 700 km s^{-1} C IV plots in Figures 3.7 and 3.8 is the difference in distance out to which we can travel from the center of a galaxy and still have a majority of the galaxies have detectable C IV gas. Over 50% of galaxies within 200 pkpc have C IV observed within the ± 350 km s^{-1}, and within the ± 700 km s^{-1} window over 50% of galaxies within 400 pkpc have C IV observed. A similar trend appears with Si IV, but with over 50% of galaxies observed with Si IV within a distance of 200 pkpc and ± 700 km s^{-1} from the center of the galaxy.

Earlier, we looked at the distribution of C IV and Si IV absorbers and observed that the full envelope of their distribution went out to 700 km s^{-1}, so it's not surprising that we see a larger fraction of galaxies with detections when we expand the search for absorbers to 700 km s^{-1}. For all four plots in Figures 3.7 and 3.8, over 75% of galaxies at impact parameters less than 100 pkpc have Si IV and C IV gas detected. While we see significant enhancement in Σ(N) for all four plots in Figures 3.7 and 3.8 at $D_{Tran} < 200$ pkpc, for both C IV plots we see C IV detections in > 25 % of galaxies in each impact parameter bin out to $D_{Tran} < 500$ pkpc, using the 350 km s^{-1} window and in all distance bins for $v < 700$ km s^{-1}. In the upcoming chapter we will discuss the possibility of this effect being due to the clustering of the CGMs from the halos of nearby galaxies.

For C IV absorbers that sit at a distance between $300 - 400$ kpc and within ± 700 km s^{-1} of the galaxy, 50% of galaxies have $\sum(N_{CIV}) > 10^{12.8}$ cm^{-2}, and when we move within 100 pkpc, 50% of galaxies in that bin have C IV absorbers $\sum(N_{CIV}) > 10^{14.1}$ cm^{-2}. In fact, over 75% of the galaxies in that bin have $\sum(N_{CIV}) > 10^{14.0}$ cm^{-2} for C IV absorbers. For the C IV absorbers within ± 350 km s^{-1} from the systemic redshift of the galaxy, 50% of galaxies within 200 pkpc have $\sum(N_{CIV}) > 10^{13.2}$ cm^{-2} and over 50% of the galaxies within 100 pkpc have $\sum(N_{CIV}) > 10^{14.0}$ cm^{-2}. Similar to the covering fraction plots above, the statistically significant enhancement of C IV extends to ≈400 pkpc, past which point the median level of $\sum(N_{CIV})$ is below the detection threshold of the data.

In Si IV, this enhancement for $\sum(N_{SiIV})$ extends out to ≈200 pkpc. Si IV absorbers within ± 700 km s^{-1} and 200 pkpc of the redshift of the galaxy have 50% of galaxies with $\sum(N_{SiIV}) > 10^{12.2}$ cm^{-2}, and within 100 pkpc the 50% statistic for total Si IV absorption in galaxies increases to $\sum(N_{SiIV}) > 10^{13.2}$ cm^{-2}. This value is very similar to the 50% statistic of $\sum(N_{SiIV}) > 10^{13.0}$ cm^{-2} for Si IV absorbers within ± 350 km s^{-1} at $D_{Tran} < 100$ pkpc.

3.3 C IV and Si IV Kinematics

Earlier we considered covering fractions as a function of distance and compared them to the distributions observed towards random lines of sight using thee BXS15 control sample. Now we look at the f_c as a function of velocity and how this changes as a function of impact parameter. The differential binning in this figure was used to obtain enough signal to visualize

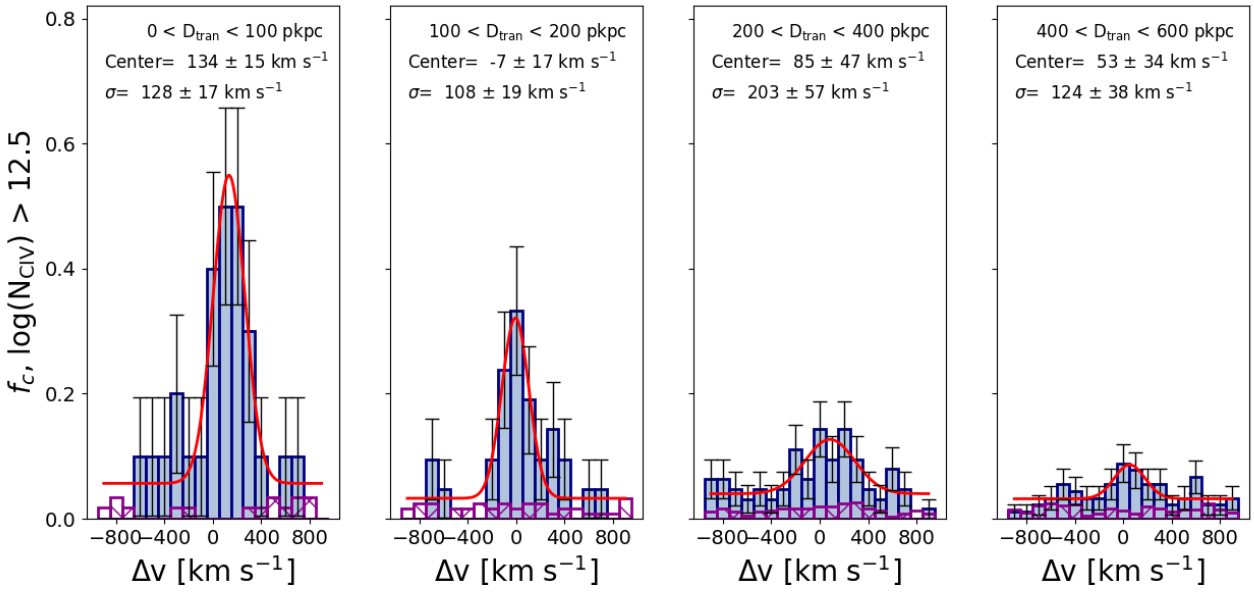

Figure 3.9: The covering fraction, f_c, of absorbers for thresholds of $\log(N_{CIV}) = 12.5$ as a function of velocity. The first two panels of the figure use D_{tran} intervals of 100 pkpc, while the last two windows use intervals of 200 pkpc. The solid blue histogram represents the covering fraction of C IV absorbers from our KBSS CGM sample, while the purple hatched histogram represents f_c at random locations in the IGM taken from BXS15. All four figures are plotted in velocity bin sizes of 100 km s^{-1}, with the center bin spanning from -50 to 50 km s^{-1}.

the distributions, and while windows 3 and 4 do show a slight peak above the floor absorption at $D_{tran} > 200$ pkpc, both windows have at most half the covering fraction as window 2. In other words, C IV absorbers are twice as likely to be found from $100 < D_{tran} < 200$ pkpc than $D_{tran} > 200$ pkpc, and three times more likely to be found at $D_{tran} < 100$ pkpc than $D_{tran} > 200$ pkpc.

At impact parameters < 200 pkpc, there is an enhancement of C IV against the leveled out IGM distances. This indicates that there is a higher probability of finding C IV absorbers as we get closer to the systemic redshift of the galaxy. While this enhancement is present for all C IV absorbers at impact parameters < 600 pkpc, the covering fraction nearly quadruples when we tighten the impact parameter threshold to < 200 pkpc. While these measurements are interesting, the most important measurement made from this figure is the velocity scales in which the enhancements are seen.

From Figure 3.9 we can clearly see an enhanced fraction of the amount of galaxies with C IV detected, near the galaxies systemic velocities. In the first panel, with galaxies at impact parameters < 100 pkpc, the center of the distribution is at 134 ± 15 km s^{-1} with the 1σ velocity dispersion of the Gaussian equal to 128 ± 17 km s^{-1}, this means that the majority of this C IV enhancement is within $0 -- 300$ km s^{-1}. When we look at the 2σ velocity dispersions for each panel of this figure we see that nearly all the signal for the normalized distribution is enclosed within, for example $2\sigma \approx 300$ km s^{-1}. The reason behind the offset from zero velocity in the < 100 pkpc bin remains unclear to us.

Quantifying the relative velocities and velocity profiles of metal enriched gas in the ionized halo of $2 \leq z \leq 2.8$ galaxies is crucial for nailing down the parameters of gas in the peak epoch of galaxy evolution. In this chapter we compared C IV and Si IV absorbers velocities and positions with respect to those of the galaxies, finding that at lower impact parameters, a higher frequency of C IV and Si IV absorbers is detected. We also see an enhancement of metal enriched gas as we approach the systemic redshifts of these galaxies. The following chapter will discuss our interpretations and the likely implications of these findings.

Conclusions

In Chapter 3, from the covering fractions in Figures 3.3 and 3.4 and total summed column density statistic plots in Figures 3.7 and 3.8 we have shown conclusive evidence that C IV and Si IV absorption along QSO sight lines is correlated with the presence of galaxies. The likelihood of seeing this absorption increases rapidly with increasing proximity to galaxies, as C IV and Si IV absorbers are clustered with galaxies.

Rudie et al. (2012) found that the most significantly enhanced H I absorption resided within transverse distances of $<\sim$ 300 pkpc and within $\pm$ 300 km s^{-1} of the system redshifts of galaxies. This put the CGM of H I at $\sim$300 pkpc, as we saw in Chapter 3 from Figures 3.3 and 3.7, the enhancement of C IV extends to $\sim$ 300$-$400 pkpc which we will now take as the defining bounds for the C IV CGM. We can also make an estimation that the Si IV CGM extends to $\sim$ 200 pkpc, determined from the sum statistic and covering fraction plots.

The column densities of H I, C IV and Si IV absorbers are strongly correlated with D_{Tran}, with the trend that a decrease in impact parameter is correlated with a rise in column densities within in the CGM. Rudie et al. (2012) considered the H I absorbers within $\pm$ 350 km s^{-1} for each of the 10 galaxies within 100 pkpc to find that the median value of N_{HI} ($10^{16.5}$ cm s^{-1}) was 3 orders of magnitude higher than at random places in the IGM. From Figure 3.7, for the C IV absorbers within $\pm$ 350 km s^{-1} from the systemic redshift of the galaxy, over 50% of the galaxies within 100 pkpc have $\sum(N_{CIV}) > 10^{14.0}$ cm^{-2}, which is more than 1 order of magnitude higher than the N_{CIV} completeness limit from IGM (N_{CIV}) $> 10^{12.5}$ cm^{-2} sample. While it is difficult to compare metal enhancements to those of the highly abundant H I, we can look at the scales at which we see N_{CIV} and N_{SiIV} increasing vs plateauing and compare those results to H I.

In our covering fraction plots from Figure 3.3, within $\pm$ 350 km s^{-1} from the systemic redshift of the galaxy and 100 pkpc for C IV, there is a factor >8 enhancement in the covering fraction of the CGM sample with respect to random lines of sight. This means that you are more than 8 times more likely to find a C IV absorber within 100 pkpc of a galaxy (within $\pm$ 350 km s^{-1}) , than in a random location in the IGM. The same conditions is true for Si IV, except that you drop from >8 times more likely to a factor >5 times more likely. While the covering fraction in the CGM tends to plateau between 300$-$400 pkpc for the C IV covering fraction plots, you are still about twice as likely to find C IV past these distances in the CGM sample than at a random sightline in the IGM. For H I , Rudie et al. (2012) also found that N_{HI} and the probability of detecting H I absorbers (covering fraction) decreased with increasing D_{Tran} to 300 pkpc, at which point the signal plateaus, but remains significantly

higher than the random sample out to 2 pMpc.

In regards to the kinematic structure of the CGM, we have demonstrated that the velocity distribution of the metal absorbers in the CGM is consistent with the dynamics, kinematics and spatial extent Rudie et al. (2012) saw with H I in the CGM/IGM. In other words, the same regions in space and velocity in which we see an enhancement of H I, also show enhanced metals absorption. After evaluating the $\sum$(HI), Rudie and collaborators hypothesized that they were seeing the clustering of other galaxies' CGM. Through the work done in this thesis, we also see gas enhancement similar to the H I in Rudie et al. 2012, but we see C IV and Si IV metal absorbers clustered on pMpc scales in excess of the IGM. Since the gas clustered on Mpc scales contains an excess quantity of ionized metals in addition to H I compared to the IGM, we expect the excess gas is due to the clustering of other metal-enriched galactic halos.

The velocity dispersion in figure 3.1 reveals the kinematic substructure of the CGM by taking into account the distribution of gas as a function of velocity. In this figure we looked at the velocity distribution scale spread, in terms of velocity dispersion and max velocity of the C IV and Si IV absorbers compared with the Rudie et al. (2012) H I absorbers velocity distribution. The distribution of relative velocities (Δv) for all 3 ions peaked near the systemic redshift of galaxies in our sample (3.1). The velocity dispersion for C IV at $D_{Tran} < 300$ pkpc is 175 km s^{-1}, and we use the 2σ distribution of that value, or 350 km s^{-1}, for many of the results in the previous chapter.

In order to get velocities higher than what gravity provides alone we need another source of energy to excite the gas beyond its gravitational potential energy. Since we know the mass of these halos, we can calculate their circular velocities via equation 3.4 (Rudie et al. 2012, Conroy et al. 2008, Adelberger et al. 2005b) and from these values we know what characteristic velocities to expected for inflowing gas due to gravity.

$$v_{cir} \quad = \sqrt{\frac{GM_{DM}}{r_{vir}}} = \quad 220 \quad \text{km} \quad \text{s}^{-1}, \tag{3.4}$$

where we assume $M_{DM} = 10^{12}$ $M_\odot$ and $r_{vir} = 91$ pkpc.

We take into account cosmic infall as a source of the measured velocity dispersion for these absorbers, but if cosmic infall was solely responsible for these velocities we would only expect a velocity up to what gravity could provide. We found the 1-sigma velocity dispersion within 100 pkpc for CIV absorbers to be > 220 km s^{-1} with the maximum velocity (V_{MAX}) for C IV at 679 km s^{-1} being much larger than the circular velocity. Additionally, 40 % of all the C IV absorbers within 100 pkpc have velocities above the 220 km s^{-1} circular velocity contribution. Since there is a significant fraction of absorbers that have velocities above the circular velocity, and the velocity we measure is a lower limit on the actual velocity dispersion (because we are only measuring the line of sight velocity as opposed to the 3D velocity dispersion) we must have some non gravitational motions. These kinematic distributions are consistent with the detection of gas that is coming out of the galaxy in a galactic wind. This galactic wind was enriched by the star formation process in the ISM of the galaxy, which led to the metal-bearing C IV and Si IV gas we are detecting.

The COSHalos survey used observations of CGM gas at $z \sim 0.2$ (Werk et al. 2013, Tumlinson et al. 2013) to measure velocity dispersions, finding that $\geq 90\%$ of the detected H I column density is confined within ± 200 km s^{-1} of the galaxies, which is less than the velocity required to escape the halo (Tumlinson, Peebles, and Werk 2017). These low$-z$ CGM studies show that most of the detected CGM absorption is consistent with being bound to the host galaxy, which imply that if there are galaxy outflows, much of the outflowing gas is being recycled. This is true for H I (Tumlinson et al. 2013), Mg II (Bergeron Boisse 1991, Johnson et al. 2015b, Nielsen et al. 2015), OVI (Tumlinson et al. 2011, Mathes et al. 2014). In Figure 3.2 we see that these high-velocity parcels of C IV and Si IV gas are moving around galaxies, we even find a handful of absorbers within 100 kpc in excess of the escape velocity boundaries. Therefore not only do we think we are detecting outflows, but in some cases we are detecting high velocity gas that is moving at a rapid enough velocity to break free of the gravitational potential of these galaxies. This scenario is consistent with the fact that we are observing galaxies near the peak of the star formation activity history of the Universe, where outflows created from this ongoing star formation are expected to be stronger and more common than at low redshift.

As we approach the CGM of star-forming, Lyman-Break galaxies we observe more gas and metals. This is not unexpected given the work from Adelberger et al. (2003, 2005a), Rudie et al. (2012) and Turner et al. (2014) showing strong correlations between the position of galaxies and the strength of H I and C IV absorption. We find a statistically significant enhancement of C IV and Si IV as a function of impact parameter out to 1.5 pMpc. Turner et al. 2014 also found metal-rich gas enhancement from their C IV covering fractions in the transverse direction out to their maximum impact parameter covered by the survey (2 pMpc).

We find the strongest enhancements of C IV absorption out to distances of 300 pkpc away from galaxies, for Si IV we only observe highly enhanced absorption out to 200 kpc. One reason for the extension of C IV being larger than Si IV is likely due to the higher ionization potential of the C IV ion itself. C IV has a higher ionization potential than Si IV by a non negligible amount, and numerical simulations show that more highly ionized gas typically has a more extended distribution in the CGM around galaxies. This is likely associate with gas at larger radii being at lower densities and therefore more easily ionized than the denser gas that lives closer to galaxies.

We don't know what part of CGM gas is ionized carbon (C II), doubly ionized carbon (C III), triply ionized carbon (C IV) or quadruply ionized carbon (C V), therefore the only way to actually determine the metallicity would be to complete the photoionization analysis of all the absorbers in this sample. In future work we want to properly characterize the abundances of the ions as a function of space and velocity around galaxies, which would require proper photoionization modeling with a software like CLOUDY. These models will take into account various systematic uncertainties we have with the degeneracies between photoionization and collisional ionization.

Once we have those measurements, we will more accurately be able to distinguish between details of different feedback models and comparisons of hydrodynamic simulations of outflows around galaxies. These measurements will be used to constrain the effects of feed-

back mechanisms on star forming galaxies and their environment during the universal peak in star formation and black hole accretion. Constraining metal distributions and gas flows is crucial to understand galaxy formation.

Bibliography

Adelberger KL, Steidel C. C. , Shapley A. E., Pettini M. 2003. ApJ 584:45–75

Adelberger, KL., Shapley, A. E., Steidel, C. C., Pettini, M., Erb, D. K., Reddy, N. A. 2005a. ApJ 629:36

Adelberger, KL., Steidel, C. C., Pettini, M., Shapley, A. E., Reddy, N. A., Erb, D. K. 2005b. ApJ 619:697

Adelberger, KL., Steidel, C. C., Shapley, A. E., Hunt, M. P., Erb, D. K., Reddy, N. A., Pettini, M. 2004. ApJ 607:226

Anglés-Alcàzar, D., Faucher-Giguère, C.-A., Kereš, D., Hopkins, P. F., Quataert, E., Murray, N. 2016. MNRAS. arXiv:1610.08523

Becker, G. D., Bolton, J. S., Haehnelt, M. G., Sargent, W. L. W. 2011a. MNRAS, 410:1096

Becker, G. D., Rauch, M., Sargent, W. L. W. 2009, ApJ. 698:1010

Becker, G. D., Sargent, W. L. W., Rauch, M., Calverley, A. P. 2011b. ApJ 735:93

Boksenberg A. and Sargent. 2015. APJ. 218:7

Bordoloi R, Heckman TM, Norman CA. 2016. ArXiv e-prints

Bordoloi R, Lilly SJ, Hardmeier E, et al. 2014a. ApJ 794:130

Bordoloi R, Lilly SJ, Knobel C, et al. 2011. ApJ 743:10

Bordoloi R, Tumlinson J, Werk JK, et al. 2014b. ApJ 796:136

Conroy, C., Shapley, A. E., Tinker, J. L., Santos, M. R., Lemson, G. 2008. ApJ, 679:1192

Chen HW, Helsby JE, Gauthier JR, et al. 2010. ApJ 714:1521–1541

Chen HW, Lanzetta KM, Webb JK, Barcons X. 1998. ApJ 498:77–94

Chen HW, Mulchaey JS. 2009. ApJ 701:1219–1242

Christensen CR, Dave R, Governato F, et al. 2016. ApJ 824:57

Churchill CW, Vander Vliet JR, Trujillo-Gomez S, et al. 2015. ApJ 802:10

Duffy, A. R., Schaye, J., Kay, S. T., Dalla Vecchia, C. 2008, MNRAS. 390:L64

Ellison, S. L., Songaila, A., Schaye, J., Pettini, M. 2000, APJ. 120:1175

Erb, D. K. 2008, ApJ. 674:151

Erb, D. K., Shapley, A. E., Pettini, M., Steidel, C. C., Reddy, N. A., Adelberger, K. L. 2006a, ApJ. 644:813

Erb, D. K., Steidel, C. C., Shapley, A. E., Pettini, M., Reddy, N. A., Adelberger, K. L. 2006b, ApJ. 647:128 —. 2006c, ApJ. 646:107

Faucher-Giguère, C.-A. Kereš, D. 2011, MNRAS. 412:L118

Faucher-Giguère, C.-A., Kereš, D., Ma, C.-P. 2011, MNRAS. 1399

Ford AB, Dave R, Oppenheimer BD, et al. 2014. MNRAS 444:1260–1281

Ford AB, Oppenheimer BD, Dave R, et al. 2013. MNRAS 432:89–112

Ford AB, Werk JK, Dave R, et al. 2016. MNRAS 459:1745–1763

Fox AJ, Bordoloi R, Savage BD, et al. 2015. ApJL 799:L7

Fox AJ, Lehner N, Tumlinson J, et al. 2013. ApJ 778:187

Haardt F, Madau P. 2001. Modelling the UV/X-ray cosmic background with CUBA. In Clusters of Galaxies and the High Redshift Universe Observed in X-rays.

Johnson SD, Chen HW, Mulchaey JS, et al. 2014. MNRAS 438:3039–3048

Kacprzak GG, Churchill CW, Steidel CC, et al. 2012. MNRAS 427:3029–3043

Keres D, Hernquist L. 2009. ApJL 700:L1–L5

Keres D, Katz N, Weinberg DH, Dave R. 2005. MNRAS 363:2–28

Kollmeier JA, Weinberg DH, Oppenheimer BD, et al. 2014. ApJL 789:L32

Muratov AL, Keres D, Faucher-Giguere CA, et al. 2016. ArXiv e-prints

Muratov AL, Keres D, Faucher-Gigu‘ere CA, et al. 2015. MNRAS 454:2691–2713

Muzahid S, Kacprzak GG, Churchill CW, et al. 2015. ApJ 811:132

Muzahid S, Srianand R, Bergeron J, Petitjean P. 2012. MNRAS 421:446–467

Navarro, J. F., Frenk, C. S., White, S. D. M. 1997, ApJ. 490:493

Nielsen NM, Churchill CW, Kacprzak GG, Murphy MT. 2013. ApJ 776:114

Nielsen NM, Churchill CW, Kacprzak GG, et al. 2015. ApJ 812:8344

Tumlinson, Peeples, Werk, Annual Review 2017. ArXiv:1709.09180v1

Nielsen NM, Churchill CW, Kacprzak GG, et al. 2016. ApJ 818:171

Oke, J. B., Cohen, J. G., Carr, M., Cromer, J., Dingizian, A., Harris, F. H., Labrecque, S., Lucinio, R., Schaal, W., Epps, H., Miller, J. 1995, PASP. 107:375

Oppenheimer BD, Crain RA, Schaye J, et al. 2016b. MNRAS 460:2157–2179

Oppenheimer BD, Dave R. 2006. MNRAS 373:1265–1292

Oppenheimer BD, Dave R. 2008. MNRAS 387:577–600

Oppenheimer BD, Dave R, Keres D, et al. 2010. MNRAS 406:2325–2338

Oppenheimer BD, Schaye J. 2013a. MNRAS 434:1063–1078

Oppenheimer BD, Schaye J. 2013b. MNRAS 434:1043–1062

Peeples MS, Werk JK, Tumlinson J, et al. 2014. ApJ 786:54

Prochaska JX, Bloom JS, Chen HW, et al. 2004. ApJ 611:200–207

Prochaska JX, Lau MW, Hennawi JF. 2014. ApJ 796:140

Prochaska JX, Weiner B, Chen HW, et al. 2011a. ApJS 193:28

Prochaska JX, Weiner B, Chen HW, et al. 2011b. ApJ 740:91

Prochaska JX, Werk JK, Worseck G, et al. 2017. ApJ 837:169

Rakic, O., Schaye, J., Steidel, C. C., Rudie, G. C. 2011a, MNRAS. 414:3265—. 2011b, ArXiv e-prints

Rauch M, Haehnelt MG. 2011. MNRAS 412:L55–L57

Rauch M, Sargent WLW, Barlow TA. 2001. ApJ 554:823–840

Rubin KHR, Hennawi JF, Prochaska JX, et al. 2015. ApJ 808:38

Rubin KHR, Prochaska JX, Koo DC, Phillips AC. 2012. ApJL 747:L26

Rubin KHR, Prochaska JX, Koo DC, et al. 2014. ApJ 794:156

Rudie GC, Steidel CC, Trainor RF, et al. 2012. ApJ 750:67

Ryan-Weber, E. V., Pettini, M., Madau, P. 2006, MNRAS. 371:L78

Ryan-Weber, E. V., Pettini, M., Madau, P., Zych, B. J. 2009, MNRAS. 395:1476

Sargent WLW, Young PJ, Boksenberg A, Tytler D. 1980. ApJS 42:41–81

Savage BD, Kim TS, Wakker BP, et al. 2014. ApJS 212:8

Savage BD, Lehner N, Narayanan A. 2011. ApJ 743:180

Schaye J, Carswell RF, Kim TS. 2007. MNRAS 379:1169–1194

Schaye J, Crain RA, Bower RG, et al. 2015. MNRAS 446:521–554

Shapley, A. E., Steidel, C. C., Pettini, M., Adelberger, K. L. 2003, ApJ. 588:65

Shapiro PR, Field GB. 1976. ApJ 205:762–765

Shen S, Madau P, Aguirre A, et al. 2012. ApJ 760:50

Shen S, Madau P, Guedes J, et al. 2013. ApJ 765:89

Simcoe, R. A. 2011, ApJ. 738:159

Simcoe, R. A., Cooksey, K. L., Matejek, M. E., Burgasser, A. J., Bochanski, J., Lovegrove, E., Bernstein, R. A., Pipher, J. L., Forrest, W. J., McMurtry, C., Fan, X., O'Meara, J. 2011. ArXiv e-prints

Simcoe, R. A., Sargent, W. L. W., Rauch, M. 2002, ApJ. 578:737

Songaila, A. Cowie, L. L. 1996, ApJ, 112, 335

Allison L. Strom and Charles C. Steidel and Gwen C. Rudie and Ryan F. Trainor and Max Pettini and Naveen A. Reddy 2017, AAS. 836:164

Steidel, C. C., Adelberger, K. L., Shapley, A. E., Pettini, M., Dickinson, M., Giavalisco, M. 2003, ApJ. 592:728

Steidel CC, Erb DK, Shapley AE, et al. 2010. ApJ 717:289–322

Steidel, C. C., Shapley, A. E., Pettini, M., Adelberger, K. L., Erb, D. K., Reddy, N. A., Hunt, M. P. 2004, ApJ. 604:534

Tripp TM, Giroux ML, Stocke JT, et al. 2001. ApJ 563:724–735

Tripp TM, Meiring JD, Prochaska JX, et al. 2011. Science 334:952

Tripp TM, Sembach KR, Bowen DV, et al. 2008. ApJ 177:39–102

Tumlinson J, Shull JM, Giroux ML, Stocke JT. 2005. ApJ 620:95–112

Tumlinson J, Thom C, Werk JK, et al. 2011. Science 334:948

Tumlinson J, Thom C, Werk JK, et al. 2013. ApJ 777:59

Turner ML, Schaye J, Crain RA, et al. 2016. MNRAS 462:2440–2464

Turner ML, Schaye J, Steidel CC, et al. 2014. MNRAS 445:794–822

Turner ML, Schaye J, Steidel CC, et al. 2015. MNRAS 450:2067–2082

van de Voort F, Schaye J, Altay G, Theuns T. 2012. MNRAS. 421:2809–2819

Werk JK, Prochaska JX, Cantalupo S, et al. 2016. ArXiv e-prints

Werk JK, Prochaska JX, Thom C, et al. 2012. ApJS 198:3

Werk JK, Prochaska JX, Thom C, et al. 2013. ApJS 204:17

Werk JK, Prochaska JX, Tumlinson J, et al. 2014. ApJ 792:8